



UPPSALA  
UNIVERSITET

*Digital Comprehensive Summaries of Uppsala Dissertations  
from the Faculty of Science and Technology 167*

# A Theoretical Study of Magnetism in Nanostructured Materials

ANDERS BERGMAN



ACTA  
UNIVERSITATIS  
UPSALIENSIS  
UPPSALA  
2006

ISSN 1651-6214  
ISBN 91-554-6527-7  
urn:nbn:se:uu:diva-6763

Dissertation presented at Uppsala University to be publicly examined in Polhemsalen, Ångströmlaboratoriet, Uppsala, Friday, May 5, 2006 at 10:15 for the degree of Doctor of Philosophy. The examination will be conducted in English.

#### **Abstract**

Bergman, A. 2006. A Theoretical Study of Magnetism in Nanostructured Materials. Acta Universitatis Upsaliensis. *Digital Comprehensive Summaries of Uppsala Dissertations from the Faculty of Science and Technology* 167. x + 78 pp. Uppsala. ISBN 91-554-6527-7.

A first-principles linear scaling real-space method for investigating non-collinear magnetic behaviour of nanostructured materials has been developed. With this method, the magnetic structures of small supported transition metal clusters have been examined. The geometric constraints imposed on the clusters by the underlying surface is found to cause non-collinear behaviour for V, Cr, and Mn clusters on Cu(111). Fe clusters supported on Cu and Ni have been studied and both spin and orbital moments are found to be enhanced for the Fe atoms, which is attributed to the reduced symmetry present at the surface. Atoms in Co clusters have been found to order antiferromagnetically, and some times in a non-collinear fashion, when deposited on a W surface. Small clusters of fcc Fe embedded in Cu have been examined and a new type of ordering, not present in larger fcc Fe systems was found.

Several theoretical studies of Fe and Co based nanostructures consisting of multilayers or embedded clusters have been conducted, with the aim of predicting high moment materials for use in data storage applications. In agreement with previous experiments an enhancement of the magnetic moment is found compared to the magnetic moment of bcc Fe. The enhancement has been shown to be caused by increased spin moments for Fe atoms in close proximity with Co atoms, and this enhancement depends on the number of Co neighbours. As a result of these studies, a possible method of increasing the magnetic moment of cluster based materials has been proposed.

Fermi surface analysis have been performed both on bulk materials, in order to investigate mechanisms for stabilizing non-collinear magnetic states, and in layered structures where the effect of the Fermi surface on the interlayer exchange coupling has been investigated.

In addition to the development of a real-space electronic structure method for non-collinear magnetism, a density matrix purification method has been implemented in the framework of linear muffin-tin orbitals.

*Keywords:* magnetism, clusters, non-collinear, multilayers, first-principles theory, electronic structure, high-moment materials, exchange interactions, linear scaling methods

*Anders Bergman, Department of Physics, Box 530, Uppsala University, SE-75121 Uppsala, Sweden*

© Anders Bergman 2006

ISSN 1651-6214

ISBN 91-554-6527-7

urn:nbn:se:uu:diva-6763 (<http://urn.kb.se/resolve?urn=urn:nbn:se:uu:diva-6763>)

*Till Peggen.*



## List of Papers

This thesis is based on the following papers, which are referred to in the text by their Roman numerals.

- I        **Linear scaling density matrix approach for the linear muffin-tin orbital method.**  
A. Bergman, E. Holmström and A.M.N. Niklasson,  
*In manuscript*
- II       **The Fermi Surface Effect on Magnetic Interlayer Coupling.**  
E. Holmström, A. Bergman, L. Nordström, S.B. Dugdale,  
I. Abrikosov and B.L. Györffy,  
*Phys. Rev. B* **70**, 064408 (2004)
- III      **The role of magnetic impurities in Fe/V multilayers.**  
B. Skubic, E. Holmström, A. Bergman and O. Eriksson,  
*In manuscript*
- IV      **Magnetism of Fe/V and Fe/Co multilayers.**  
O. Eriksson, L. Bergqvist, E. Holmström, A. Bergman,  
O. LeBacq, S. Frota-Pessôa, B. Hjörvarsson and L. Nordström,  
*J. Phys.: Condens. Matter* **15** S599, (2003)
- V        **Magnetic properties of Fe/Co(001) superlattices from first-principles theory.**  
A. Bergman, T. Burkert, B. Sanyal, S. Frota-Pessôa,  
L. Nordström, A. V. Ruban, S. I. Simak and O. Eriksson,  
*Submitted to Phys. Rev. B*
- VI      **Local magnetic effects of interface alloying in Fe/Co multilayers.**  
S. Kamali-M, A. Bergman, G. Andersson, V. Stanciu and L. Häggström,  
*Submitted to J. Phys.: Condens. Matter*
- VII     **Magnetism of Fe clusters embedded in a Co matrix from first-principles theory.**  
A. Bergman, E. Holmström, A.M.N. Niklasson, L. Nordström,  
S. Frota-Pessôa and O. Eriksson,  
*Phys. Rev. B* **70** 174446 (2004)
- VIII    **Magnetic moments of Fe clusters embedded in an FeCo alloy.**  
A. Bergman and O. Eriksson,  
*Submitted to Phys. Rev. B*

- 
- IX      **Conditions for noncollinear instabilities of ferromagnetic materials.**  
R. Lizárraga, L. Nordström, L. Bergqvist, A. Bergman, E. Sjöstedt, P. Mohn and O. Eriksson,  
*Phys. Rev. Lett.* **91** 107205 (2004)
- X        **A theoretical and experimental study of the magnetic structure of  $\text{TlCo}_2\text{Se}_2$ .**  
R. Lizárraga, S. Ronneteg, R. Berger, A. Bergman, O. Eriksson and L. Nordström,  
*Phys. Rev. B* **70**, 024407 (2004)
- XI      **A crystal and magnetic structure investigation of  $\text{TbNi}_{5-x}\text{Cu}_x$  ( $x = 0, 0.5, 1.0, 1.5, 2.0$ ); Experiment and Theory**  
R. Lizárraga, A. Bergman, T. Björkman, H-P. Liu, Y. Andersson, T. Gustafsson, A.G Kuchin, A.S Ermolenko, L. Nordström and O. Eriksson,  
*In Manuscript*
- XII     **Magnetic structure of a small fcc Fe cluster in Cu.**  
A. Bergman, R. Robles and L. Nordström,  
*In Manuscript*
- XIII    **Magnetic interactions of Mn clusters supported on Cu.**  
A. Bergman, L. Nordström, A. B. Klautau, S. Frota-Pessôa and O. Eriksson,  
*Submitted to Phys. Rev. B*
- XIV    **Magnetic structure of Fe, Cr, and Mn clusters supported on Cu(111).**  
A. Bergman, L. Nordström, A. B. Klautau, S. Frota-Pessôa and O. Eriksson,  
*In manuscript*
- XV     **Non-collinear magnetisation of V clusters supported on a Cu (111) surface: theory.**  
A. Bergman, L. Nordström, A. B. Klautau, S. Frota-Pessôa and O. Eriksson,  
*Submitted to Surf. Sci.*
- XVI    **Magnetism of Co overlayers and nanostructures on W(001): A first principles study.**  
A. Bergman, L. Nordström, A. B. Klautau and O. Eriksson,  
*In Manuscript*
- XVII   **Spin and orbital moments of Fe clusters supported on Ni(001).**  
R. Robles, A. Bergman, A. B. Klautau, O. Eriksson and L. Nordström,  
*In Manuscript*

- XVIII      **A first principles study of the magnetism and electronic structure of Cr clusters supported on a Au (111) surface.**  
A. Bergman, L. Nordström, A. B. Klautau, S. Frota-Pessôa and  
O. Eriksson,  
*In Manuscript*



# Contents

1	Introduction	1
2	Density Functional Theory	3
2.1	The many-body problem	3
2.2	Density Functional Theory	3
2.3	Local Density Approximation	4
2.4	Spin polarized systems	4
2.5	Spin-orbit coupling	6
3	Linear Muffin-tin Orbitals	7
3.1	The eigenvalue problem	7
3.2	The LMTO basis set	7
3.3	Atomic sphere approximation	9
3.4	Representations	10
3.5	The Hamiltonian	12
4	The recursion method	13
4.1	The chain model	13
4.2	Calculation of the recursion parameters	15
4.3	The continued fraction	16
4.4	Self consistency	18
4.5	Non-collinear magnetism	19
4.6	Spin-orbit coupling	21
4.7	O(N) with Density Matrix Purification	22
4.7.1	Trace correcting purification	23
4.7.2	Trace resetting purification	23
4.7.3	LMTO self-consistency	24
5	Magnetic ordering	27
5.1	The Stoner criterion	28
5.2	Magnetic susceptibility and nesting	30
5.3	Exchange interactions	32
5.4	Interlayer exchange coupling	32
6	High moment materials	35
6.1	Material prerequisites for data storage	35
6.2	Bulk Fe-Co alloys	36
6.3	Artificial structures	37
6.4	Multilayers	38
6.4.1	Magnetic moments	38
6.4.2	Hyperfine fields	39

6.4.3	Interface roughness	40
6.5	Embedded clusters	42
6.5.1	Modelling the maximum moment	46
6.5.2	Alloying the embedding matrix	47
7	Non-collinear magnetism	51
7.1	Criteria for non-collinear magnetism	51
7.2	TiCo <sub>2</sub> Se <sub>2</sub>	53
7.3	TbNi <sub>5</sub>	53
7.4	Fcc Fe	54
8	Magnetic nanostructures	59
8.1	Reduced dimensionality	59
8.2	Frustration	61
8.3	Substrates	62
8.4	Cr, Mn, and Fe on Cu(111)	63
8.5	V on Cu(111)	66
8.6	Co on W(001)	67
8.7	Cr on Au(111)	68
9	Perspectives and outlook	69
10	Sammanfattning	71
11	Acknowledgements	73

# 1. Introduction

This thesis consist of roughly  $4 \cdot 10^{25}$  atoms. The vast majority of these atoms are surrounded by so many other similar atoms that they are bulk like, i.e. they are happily unaware of that this book is indeed not infinitely thick. If the dimensions of this thesis would decrease, more and more of the atoms would start to notice the effects of the interface between the papers and the surrounding. Eventually no atom would longer be in a bulk like surrounding and the behaviour of the atoms will thus be different. Exploiting the fact, that atoms in systems where at least one dimension is in the nanometer scale have different properties than in bulk systems, is the essence of nanotechnology.

In 1959, the demigod of physics Richard Feynman, gave a talk on the topic “There is plenty of room at the bottom”, which virtually jump-started the field of nanotechnology. Now, half a decade later, this field is hotter than ever. Fueled by scientific curiosity and the search for novel materials with improved properties, experimental techniques that can manipulate single atoms have been developed and deposition processes have been refined so that it is now possible to construct nanostructured materials consisting of small clusters, or multilayers with thicknesses of a few atomic monolayers. These experimental developments allow for new possibilites for constructing materials with tailored properties, by controlling their chemical composition and their structure.

In order to fully exploit the possibilites of nanostructured materials, well-founded understanding of their behaviour is needed. This understanding can be obtained either from experimental analysis or from quantum mechanical calculations. Density functional theory (DFT) have during the last decades, proved to be a valuable tool for such purposes. Based entirely on quantum mechanics, DFT can in principle calculate the electronic state of a system given no more information than the atomic number of the atoms, and often also the structure of the system.<sup>1</sup> Using methods based on DFT, the properties of nanosystems can thus be calculated. However, many of these methods rely on the approximation that the system is indeed bulk like and infinite, by using periodic boundary conditions, which renders these method less effective for treating systems that lack translational symmetry.

---

<sup>1</sup>Since DFT yields an approximate solution to the full many-body problem of the system, it is not always as accurate as one would wish. The shortcomings of DFT is not a major part of this thesis, but is discussed to some extent in Chapter 2

This thesis is focused on theoretical calculations of the magnetic properties of nanosized systems. The calculations have mostly been performed with a real-space recursion method that does not need periodic boundary conditions and is thus well suited to treat nanostructured materials. The method, has been extended so that more general magnetic configurations, i.e. non-collinear magnetism, can be treated.

The non-collinear implementation has been applied to calculate the magnetic structure of small metal clusters deposited on metal surfaces. The behaviour of small magnetic clusters make them interesting as possible candidates for future recording media, where each cluster can hypothetically store one bit of information by means of the magnetic configuration. The geometries of the clusters also allow for experimental analysis using scanning tunneling microscopy which makes it possible to benchmark the accuracy of the theoretical method. The magnetic structure of small, fcc structured, iron clusters embedded in copper, which are known to exhibit non-collinear ordering, has also been examined with the newly developed method

An important strength of electronic calculations is that they can not only be used to reproduce experimental findings but can also be used to predict new materials with novel properties. Nanostructured materials, such as multilayers or cluster based materials consisting of iron and cobalt have been proposed as possible candidates for a high moment material. Such materials are highly sought after for use in write heads in hard drives, since a high moment material can create a high magnetization density which allows for more stable recording media which in turn can be used to increase the storage density of current hard drives. Several studies of such systems are presented within this thesis.

The first part of this thesis is devoted to the theoretical background to the calculational method used for the studies of the nanostructured systems. In Chapter 2 a brief introduction to DFT is given. Chapter 3 describes the formalism of linear muffin-tin orbitals which are used as an efficient basis set. In Chapter 4 the actual method is presented, with emphasis on the non-collinear implementation.

A large part of this thesis focuses on the magnetic ordering of different materials, and in Chapter 5 the mechanism that cause materials to order magnetically are reviewed. The treatment of magnetic ordering continues in Chapter 7 where criteria for stabilizing non-collinear magnetism are presented and also discussed in terms of two different compounds. In that chapter, the examination of the magnetic structure of a fcc iron cluster embedded in copper is presented as well. Chapter 6 covers the studies of iron and cobalt systems with the goal of finding high moment materials. The chapter also includes a short introduction to different aspects of materials properties that are sought for in data storage applications. The magnetic structure of supported nanoclusters are examined in Chapter 8 together with a presentation of important concepts in nanomagnetism.

## 2. Density Functional Theory

### 2.1 The many-body problem

According to quantum mechanics, the information of the behaviour of any system of electrons and atomic nuclei is contained in the many-body wavefunction,  $\Psi$ , which can be obtained by solving the Schrödinger equation

$$\mathbf{H}\Psi = E\Psi, \quad (2.1)$$

where  $\mathbf{H}$  is the Hamiltonian operator of the system and  $E$  is the total energy. The Hamiltonian operator can be written (using atomic units) as

$$\mathbf{H} = -\sum_i \frac{\nabla_{\mathbf{R}_i}^2}{M_i} + \sum_{i \neq j} \frac{Z_i Z_j}{|\mathbf{R}_i - \mathbf{R}_j|} - \sum_i \nabla_{\mathbf{r}_i}^2 + \sum_{i \neq j} \frac{1}{|\mathbf{r}_i - \mathbf{r}_j|} - \sum_{i,j} \frac{2Z_i}{|\mathbf{r}_i - \mathbf{R}_j|} \quad (2.2)$$

where  $\mathbf{R}$  and  $\mathbf{r}$  are the coordinates for each nucleus and electron,  $Z$  denotes the atomic number for each atom and  $M$  is the mass of each nucleus. The first and third terms are the kinetic energy operators for the nuclei and electrons respectively. The remaining terms are the Coulombic nuclei-nuclei, electron-electron and electron-nuclei interactions. Since the Schrödinger equation for the full Hamiltonian is in fact impossible to solve exactly for systems of more than 2 particles, approximations must be introduced to simplify the problem. The Born-Oppenheimer approximation is a fundamental approximation based on the fact that the nuclei are much heavier than the electrons and therefore, the motion of the electrons can be decoupled from the motion of the nuclei. Even though the Born-Oppenheimer approximation gives a less complicated Hamiltonian for the electrons, the problems of the electron-electron interactions are still there and further steps need to be taken in order to achieve an efficient solution to this many-body problem.

### 2.2 Density Functional Theory

The theorem of Hohenberg and Kohn [1] states that the total energy of a many-electron system is uniquely described by its electron density and has its minimum at the ground-state density. This theorem is the foundation of Density Functional Theory (DFT) which gives us the means to reduce the complicated many-body problem to that of finding the ground state electron density. Kohn and Sham [2] have shown that instead of solving the many-body Schrödinger

equation in Eqn. 2.1, one needs to solve a single-particle equation which is referred to as the Kohn-Sham equation<sup>1</sup>.

$$[-\nabla^2 + v_{eff}(\mathbf{r})]\psi_i(\mathbf{r}) = \varepsilon_i\psi_i(\mathbf{r}). \quad (2.3)$$

The effective potential  $v_{eff}$  has then the form

$$v_{eff} = v_{ext} + 2 \int \frac{n(\mathbf{r}')}{|\mathbf{r} - \mathbf{r}'|} d\mathbf{r}' + v_{xc}(\mathbf{r}), \quad (2.4)$$

where  $v_{ext}$  is the external potential from the nuclei, the second term is the Coulomb interaction with the electron charge density and the third term is the exchange-correlation potential. The effective potential is a function of the electron density. Since the density itself is a function of the one-particle wave functions  $\psi_i$ , the Kohn-Sham equations need to be solved iteratively until the solution is self-consistent.

### 2.3 Local Density Approximation

All of the many-body effects from the original problem are now incorporated in the exchange-correlation term. Unfortunately, neither exchange nor correlation interactions can be described exactly within DFT, for real materials, so these terms need to be modelled somehow. One simple, yet surprisingly efficient, way to model the exchange-correlation potential is to treat it as the potential of an homogeneous but interacting electron gas. This is called the local density approximation (LDA) which is probably the most common exchange-correlation approximation and works best if the density of the treated system is only slowly varying. A refined model can be done by treating the exchange-correlation potential as a function of not only the electron density but also the gradient of the density, this is called the generalised gradient approximation (GGA). Despite the fact that GGA should be a better model than LDA, since it makes use of more information of the electron density, the use of GGA does not always increase the accuracy of the results. Within both LDA and GGA there exist several different parametrisation which are mostly based on quantum Monte Carlo calculations.

### 2.4 Spin polarized systems

The treatment of the electron density has, in the previous sections, only concerned non-spin-polarized systems. However the local density approximation can be extended to handle spin polarized charge densities[4](LSDA) as well.

<sup>1</sup>For a detailed derivation of the Kohn-Sham equation, c.f. Ref.[3]

In the spin polarised case, the density  $n(\mathbf{r})$  is replaced with a generalized density matrix,  $\rho(\mathbf{r})$ , as

$$n(\mathbf{r}) \implies \rho(\mathbf{r}) = \frac{n(\mathbf{r})}{2} \mathbf{1} + \frac{\mathbf{m}(\mathbf{r})}{2} \boldsymbol{\sigma}, \quad (2.5)$$

where  $\mathbf{1}$  is the 2x2 unit matrix,  $\mathbf{m}$  the magnetization density and  $\boldsymbol{\sigma} = (\sigma_x, \sigma_y, \sigma_z)$  are the Pauli spin matrices. The corresponding wave functions,  $\psi_i(\mathbf{r})$ , are then represented by spinors on the form of

$$\psi_i(\mathbf{r}) = \begin{pmatrix} \alpha_i(\mathbf{r}) \\ \beta_i(\mathbf{r}) \end{pmatrix}, \quad (2.6)$$

where  $\alpha_i(\mathbf{r})$  and  $\beta_i(\mathbf{r})$  are the spin projections. The density matrix is expressed in terms of the spinors as

$$\rho(\mathbf{r}) = \sum_{i=1}^N \begin{pmatrix} |\alpha_i(\mathbf{r})|^2 & \alpha_i(\mathbf{r})\beta_i(\mathbf{r})^* \\ \alpha_i(\mathbf{r})^*\beta_i(\mathbf{r}) & |\beta_i(\mathbf{r})|^2 \end{pmatrix}. \quad (2.7)$$

The charge and magnetization densities are then expressed as

$$n(\mathbf{r}) = Tr(\rho(\mathbf{r})) = \sum_{i=1}^N |\psi_i(\mathbf{r})|^2, \quad \mathbf{m}(\mathbf{r}) = \sum_{i=1}^N \psi_i(\mathbf{r})^\dagger \boldsymbol{\sigma}(\mathbf{r}) \psi_i(\mathbf{r}), \quad (2.8)$$

where N is the number of states for the system. Analogous to the density, the external potential is also expanded to a 2x2 matrix and the non-magnetic Kohn-Sham equation in Eqn. 2.3 can then be generalized[5] to

$$\sum_{\beta} \left( -\delta_{\alpha\beta} \nabla^2 + v_{\text{eff}}^{\alpha\beta}(\mathbf{r}) \right) \psi_{i\beta}(\mathbf{r}) = \epsilon_i \delta_{\alpha\beta} \psi_{i\beta}(\mathbf{r}) \quad \alpha = 1, 2. \quad (2.9)$$

By decomposing the effective potential,  $v_{\text{eff}}$ , into a magnetic part,  $\mathbf{b}$ , and a non-magnetic part  $v_{\text{NM}}$ , the Kohn-Sham Hamiltonian for a spin dependent system can in the LSDA be written on a similar form as the density, so that

$$\mathbf{H} = (-\nabla^2 + v_{\text{NM}}) \mathbf{1} + \mathbf{b} \cdot \boldsymbol{\sigma}. \quad (2.10)$$

The non-magnetic part of the Hamiltonian is diagonal and if the system is collinear, i.e. has a global magnetization axis, the spin dependent part can also be obtained in a diagonal form. Since the Hamiltonian is diagonal in spin-space in the collinear case, the two different spin projections can not hybridize with each other and can thus be solved independently.

When no unique global spin quantization exists, the magnetism is said to be non-collinear. Depending on the degree of approximation, the non-collinear magnetization can either be treated as a vector field, allowing for intraatomic non-collinearity[6], or only considering interatomic non-collinearity. In the latter case, each atom has a unique spin quantization axis. Within each atomic sphere, the effective potential matrix can be transformed, in a local frame of reference, to be diagonal along the local quantization axis.

In Chapter. 4, treatment of non-collinear spin densities in electronic structure calculations will be discussed further.

## 2.5 Spin-orbit coupling

The LSDA Hamiltonian in Eqn. 2.10 does only incorporate scalar relativistic effects. However, in order to calculate orbital moments and magnetic anisotropies, the relativistic spin-orbit coupling must be taken into account. This can be done by either solving the spin polarized Dirac equation, or by adding a spin-orbit term to the scalar relativistic Hamiltonian[7–9], where the spin-orbit contribution is treated self-consistently at each variational step, in accordance to

$$\mathbf{H} = \mathbf{H}_{SR} + \xi \mathbf{L} \cdot \mathbf{S}, \quad (2.11)$$

where  $\mathbf{H}_{SR}$  is the scalar relativistic Hamiltonian and  $\xi$  is the spin-orbit coupling strength

$$\xi \propto \frac{1}{r} \frac{\partial V}{\partial r}, \quad (2.12)$$

which is depending on the atomic number and the spin-orbit effect is thus larger for heavier elements. If the spin-orbit term is added to the Hamiltonian, it accounts for the interactions corresponding to Hund's third rule. In order to incorporate the effects from Hund's second rule, an orbital polarization[10, 11] effect can be introduced, by taking the following energy term

$$\mathbf{E}_{OP} = -\frac{1}{2}BL^2, \quad (2.13)$$

where B is the Racah parameter, into account.

## 3. Linear Muffin-tin Orbitals

### 3.1 The eigenvalue problem

As shown in the previous chapter, density functional theory reduces the many body problem into solving the effective one-electron wavefunctions in the Kohn-Sham equation. The most common way to solve the Kohn-Sham equation is to express the wavefunction,  $\psi$  in a suitable finite basis set,  $\{\chi_i\}$  as follows

$$|\psi\rangle = \sum_i u_i |\chi_i\rangle. \quad (3.1)$$

With this expansion, it is easy to express the wavefunction by only using the coefficient vector  $\{u_i\}$ , or in an algebraic form  $\mathbf{u}$ . This can be used to transform the Kohn-Sham equations into a generalised matrix eigenvalue problem,

$$(\mathbf{H} - \epsilon \mathbf{O})\mathbf{u} = 0 \quad (3.2)$$

where  $\mathbf{H}$  is the Hamiltonian matrix and  $\mathbf{O}$  is the overlap matrix whose matrix indices are defined as

$$\begin{aligned} \mathbf{H}_{ij} &= \langle \chi_i | H | \chi_j \rangle \\ \mathbf{O}_{ij} &= \langle \chi_i | \chi_j \rangle. \end{aligned} \quad (3.3)$$

There exists a wide variety of basis sets, each with their own advantages and shortcomings. For the purposes of the calculations included in this work, a localized and efficient basis is needed, which can be obtained with a basis set consisting of linearized muffin-tin orbitals (LMTO). In this chapter, we will deduce the basis set and also show how the LMTO basis can be transformed between orthogonal and tight-binding representations. We will also show how to construct the Hamiltonian for solving the eigenvalue problem within the LMTO method.

### 3.2 The LMTO basis set

The LMTO basis set can be constructed by considering a muffin-tin potential  $V_{MT}(\mathbf{r})$  which is described by an spherical symmetric potential  $V(r)$  within a radius  $S$  of an atomic position, and is constant and equal to the muffin-tin zero,  $V_{MTZ}$  outside the radius. A single muffin-tin potential can then be written as

$$V_{MT}(\mathbf{r}) = \begin{cases} V(r) & r \leq S \\ V_{MTZ} & r \geq S \end{cases} \quad (3.4)$$

where  $S$  is called the muffin-tin radius and  $r = |\mathbf{r} - \mathbf{R}|$ . Consider the Kohn-Sham equation for a single muffin-tin well centred at position  $\mathbf{R}$  which is embedded in the muffin-tin zero potential.

$$[-\nabla^2 + V_{MT}(\mathbf{r})] \varphi_{\mathbf{R}}(\mathbf{r}, \varepsilon) = \varepsilon \varphi_{\mathbf{R}}(\mathbf{r}, \varepsilon). \quad (3.5)$$

Since the muffin-tin potential is spherically symmetric, the solution can be separated into an angular dependent part and a radial dependent part, so that

$$\varphi_{\mathbf{R}L}(\mathbf{r}, \varepsilon) = \varphi_{\mathbf{R}l}(r, \varepsilon) Y_L(\hat{r}), \quad (3.6)$$

where  $Y_L(\hat{r})$  is a spherical harmonic with the  $l, m$  quantum numbers combined into the angular-momentum index  $L = \{l, m\}$  and the radial solution  $\varphi_{\mathbf{R}l}(r, \varepsilon)$  is given by the radial Schrödinger equation, which can be solved by numerical methods.

So far, the basis functions are energy dependent. This means that in order to get accurate solutions to the Schrödinger equation, it must be evaluated at a large number of energies which decreases the efficiency. However, as pointed out by Andersen[7], the higher order energy derivatives of the radial wavefunctions have small amplitudes. This makes it possible to expand the radial solutions with a Taylor expansion and only include the first order term.

$$\varphi_{\mathbf{R}l}(r, \varepsilon) \approx \varphi_{\mathbf{R}l}(r, \varepsilon_v) + (\varepsilon - \varepsilon_v) \dot{\varphi}_{\mathbf{R}l}(r, \varepsilon_v), \quad (3.7)$$

where  $\dot{\varphi}$  is the energy derivative at a chosen energy  $\varepsilon_v$ , which is often selected to be at the center of the band.

In the region outside of the muffin-tin well, where the potential is constant, the solutions are determined by the Helmholtz equation. If the energy is the same as the muffin-tin zero<sup>1</sup>, so that  $V_{MTZ} - \varepsilon = 0$ , then the equation has two linearly independent solutions, which can be taken as the spherical Bessel  $J_{\mathbf{R},l}(r)$  and Neumann  $K_{\mathbf{R},l}(r)$  functions given as

$$\begin{cases} J_{\mathbf{R}l} = \frac{1}{2(2l+1)} \left(\frac{r}{S}\right)^l \\ K_{\mathbf{R}l} = \left(\frac{S}{r}\right)^{l+1} \end{cases}. \quad (3.8)$$

We can now combine the solutions for the single muffin-tin potential outside and inside of the muffin-tin radius,  $S$ .

$$\varphi_{\mathbf{R}L}(\mathbf{r}, \varepsilon) \approx \begin{cases} \varphi_{\mathbf{R}l}(r, \varepsilon_v) + (\varepsilon - \varepsilon_v) \dot{\varphi}_{\mathbf{R}l}(r, \varepsilon_v) & r \leq S \\ K_{\mathbf{R}l} Y_L(r) & r > S \end{cases} \quad (3.9)$$

The irregular Neumann function  $K_{\mathbf{R}l}$ , which goes to zero at infinity, acts as an envelope function outside the muffin-tin. Inside the muffin-tin, the subscript

<sup>1</sup>This particular choice of constant energy outside the muffin-tin radius is not necessary, but simplifies the problem, and is one of the approximations included in the treatment of the muffin-tin orbitals in an atomic sphere approximation (ASA).

$v$  denotes that the energy is calculated at the energy  $\varepsilon_v$ . The solutions inside and outside of the muffin-tin can then be put together smoothly by choosing appropriate linear combinations of  $\varphi$  and  $\dot{\varphi}$  so that the wavefunction and its first derivative are continuous at the muffin-tin boundary. This is true for the muffin-tin orbital,

$$\chi_{\mathbf{RL}}(\mathbf{r}, \varepsilon) = \begin{cases} \{\varphi_v, \dot{\varphi}_v\}_{\mathbf{RL}}^{-1} [\{K, \dot{\varphi}_v\}_{\mathbf{RL}} \varphi_{\mathbf{RL}v} - \{K, \varphi_v\}_{\mathbf{RL}} \dot{\varphi}_{\mathbf{RL}v}] & r \leq S \\ K_{\mathbf{RL}} & r > S \end{cases}, \quad (3.10)$$

where  $\{\varphi_v, \dot{\varphi}_v\}_{\mathbf{RL}}$ ,  $\{K, \dot{\varphi}_v\}_{\mathbf{RL}}$  and  $\{K, \varphi_v\}_{\mathbf{RL}}$  are the Wronskians calculated at the muffin-tin radius,  $S$ , centered at the atomic positions,  $\mathbf{R}$  for the energy  $\varepsilon_v$ . A Wronskian is defined as

$$\{f, g\} = r^2 [f(r)g'(r) - f'(r)g(r)] \quad (3.11)$$

and ensures the continuity at the muffin-tin boundary. The linearized muffin-tin orbitals, written in Eqn. 3.10, form a set of minimal, atomic centered basis functions, that are almost energy independent around a given energy  $\varepsilon_v$ . Hence they form a basis set well adapted for solving the Kohn-Sham equations for crystals.

### 3.3 Atomic sphere approximation

If the system is a periodic close packed crystal, the whole crystal can be approximated as being filled with muffin-tin spheres with radii chosen so that the volume of one sphere is equal to the atomic volume. The muffin-tin spheres are overlapping to some extent, and the interstitial parts are neglected. This approximation together with the aforementioned energy-independent solution outside the muffin-tin spheres are included in the atomic sphere approximation (ASA). This is an approximation that works well for close packed systems and has the advantages of being efficient and physically transparent. For structures that lack close packing, so called empty spheres can be included at well chosen positions to decrease the overlap and simulate a close packed structure. In the ASA, the irregular envelope function  $K_{\mathbf{RL}}$  of a muffin-tin orbital centered at  $\mathbf{R}$  can be expressed inside a neighbouring sphere centered at  $\mathbf{R}'$  in terms of regular (Bessel) functions  $J_{\mathbf{R}'L}$  as

$$K_{\mathbf{RL}}(\mathbf{r}_{\mathbf{R}}) = - \sum_{\mathbf{R}'L'} S_{\mathbf{RL},\mathbf{R}'L'} J_{\mathbf{R}'L}(\mathbf{r}_{\mathbf{R}'}) \quad (3.12)$$

where  $\mathbf{r}_{\mathbf{R}} = \mathbf{r} - \mathbf{R}$ ,  $\mathbf{r}_{\mathbf{R}'} = \mathbf{r} - \mathbf{R}'$  and  $r_{\mathbf{R}'} < S_{\mathbf{R}'}$ . The expansion coefficients  $S_{\mathbf{RL},\mathbf{R}'L'}$  are referred to as the structure constants since it can be shown that they only depend on the crystal structure.

Furthermore, we can expand the envelope function  $K_{\mathbf{RL}}(\mathbf{r}_{\mathbf{R}})$  in terms of linear combinations of  $\varphi_{\mathbf{RL}v}(\mathbf{r})$  and  $\dot{\varphi}_{\mathbf{RL}v}(\mathbf{r})$ , by matching the regular expansion functions  $J_{\mathbf{R}'L}(\mathbf{r}_{\mathbf{R}'})$ , centered on off-site positions, to  $\varphi_{\mathbf{R}'L'v}(\mathbf{r}_{\mathbf{R}'})$  and

$\phi_{\mathbf{R}'L'v}(\mathbf{r}_{\mathbf{R}'})$ . The envelope function  $K_{\mathbf{R}L}(\mathbf{r}_{\mathbf{R}})$  can with the use of Wronskians be written as

$$K_{\mathbf{R}L}(\mathbf{r}_{\mathbf{R}}) = -\sum_{L'} S_{\mathbf{R}L, \mathbf{R}'L'} [\{J_{\mathbf{R}'L'}, \phi_v\}_{\mathbf{R}'L'} \phi_{\mathbf{R}'L'v}(\mathbf{r}_{\mathbf{R}'}) - \{J_{\mathbf{R}'L'}, \phi_v\}_{\mathbf{R}'L'} \phi_{\mathbf{R}'L'v}(\mathbf{r}_{\mathbf{R}'})]. \quad (3.13)$$

Substituting 3.13 in to equation 3.10 gives us the muffin-tin orbitals expressed in terms of  $\phi_{\mathbf{R}Lv}(\mathbf{r})$  and  $\phi_{\mathbf{R}'L'v}(\mathbf{r}_{\mathbf{R}'})$ .

### 3.4 Representations

The LMTO basis can be represented in different ways, each having its own special properties. Two of the most used representations are the orthogonal representation and the tight-binding representation, which has screened structure constants so that they are short-ranged. As we will show later on, the 'nearsightedness' of the tight-binding representation makes it a suitable choice for using in the recursion method (c.f. Chapter 4). However, the use of an orthogonal representation simplifies the eigenvalue problem so in order to get an optimal basis, we want to use an orthogonal representation of the LMTO-ASA, but express the Hamiltonian in tight-binding parameters. In the following section we will briefly show how this can be done. For more details, see Ref. [12]. Using bra-ket notation, we can write the expansion of the envelope function, extended over all space,  $|\mathbf{K}\rangle^\infty$ , as

$$|\mathbf{K}\rangle^\infty = |\mathbf{K}\rangle - |\mathbf{J}\rangle \mathbf{S}. \quad (3.14)$$

Since linear combinations of  $|\mathbf{K}\rangle$  and  $|\mathbf{J}\rangle$  are solutions to the Helmholtz equation, we can mix an amount  $\alpha$  of irregular  $|\mathbf{K}\rangle$  solutions to the regular  $|\mathbf{J}\rangle$  solutions and get

$$|\mathbf{J}^\alpha\rangle = |\mathbf{J}\rangle + \alpha |\mathbf{K}\rangle. \quad (3.15)$$

This mixing of solutions can be seen as a screening of the envelope function by adding multipoles on neighbouring spheres. Combining Eqn. 3.14 and Eqn. 3.15, we get the screened envelope function  $|\mathbf{K}^\alpha\rangle^\infty$  as

$$|\mathbf{K}^\alpha\rangle^\infty = |\mathbf{K}\rangle - |\mathbf{J}^\alpha\rangle \mathbf{S}^\alpha. \quad (3.16)$$

The new screened structure constants  $\mathbf{S}^\alpha$  are related to the bare (canonical) structure constants,  $\mathbf{S}$ , as

$$\mathbf{S}^\alpha = \mathbf{S}(1 - \alpha \mathbf{S}). \quad (3.17)$$

Optimal values of  $\alpha$  that limits the range of  $\mathbf{S}^\alpha$  to essentially second nearest neighbours have been found empirically[13]. These values of  $\alpha$  gives

the tight-binding representation of the LMTO basis (TB-LMTO), with the screened structure constants  $\bar{\mathbf{S}}$ .<sup>2</sup>

According to Eqn. 3.10 and Eqn. 3.13 we can write the basis function  $|\chi\rangle$  as a linear combination of  $|\varphi\rangle$  and  $|\phi\rangle$ . In a similar fashion, the screened basis function  $\chi_{\mathbf{RL}}^{\alpha\infty}$ , extending over the whole space, can be expressed in terms of  $\varphi_{\mathbf{R}/V}(\mathbf{r})$  and  $\phi_{\mathbf{RL}V}(\mathbf{r})$  which can be written as

$$|\chi^{\alpha}\rangle^{\infty} = |\varphi\rangle + |\phi^{\alpha}\rangle \mathbf{h}^{\alpha} \quad (3.18)$$

with

$$|\phi^{\alpha}\rangle = |\phi\rangle + |\varphi\rangle \mathbf{o}^{\alpha} \quad (3.19)$$

where the matrix  $\mathbf{h}^{\alpha}$  is obtained in the augmentation process determined from the expansion of the envelope function, and  $\mathbf{o}^{\alpha}$  ensures the smoothness of the augmentation. Within this choice of basis  $\alpha$ , the Hamiltonian  $\mathbf{H}^{\alpha}$  and the overlap matrix  $\mathbf{O}^{\alpha}$ , defined in Eqn. 3.3 is given by

$$\begin{cases} \mathbf{H}^{\alpha} = \langle \chi^{\alpha} | H | \chi^{\alpha} \rangle = \mathbf{h}^{\alpha} (1 + \mathbf{o}^{\alpha} \mathbf{h}^{\alpha}) + \varepsilon_V \mathcal{O}^{\alpha} \\ \mathbf{O}^{\alpha} = \langle \chi^{\alpha} | \chi^{\alpha} \rangle = (1 + \mathbf{o}^{\alpha} \mathbf{h}^{\alpha}) (\mathbf{o}^{\alpha} \mathbf{h}^{\alpha} + 1) \end{cases} \quad (3.20)$$

where we have used the relations

$$\begin{aligned} \langle \varphi | \varphi \rangle &= 1 & \langle \varphi | \phi^{\alpha} \rangle &= \mathbf{o}^{\alpha} & \langle \varphi | \phi \rangle &= 0 \\ \langle \phi | \phi \rangle &= \mathbf{p} & \langle \phi^{\alpha} | \phi^{\alpha} \rangle &= \mathbf{p}^{\alpha} = \mathbf{o}^{\alpha} + \mathbf{p} \end{aligned} \quad (3.21)$$

and actually neglected the small parameter  $\mathbf{p}$ .

If the screening  $\alpha$  is now chosen as a particular value  $\gamma$  so that  $\mathbf{o}^{\gamma}$  becomes zero, the overlap matrix becomes the identity matrix and the basis is orthogonal. The Hamiltonian in this orthogonal representation is easily written as

$$\mathbf{H}^{\gamma} = \mathbf{h}^{\gamma} + \varepsilon_V. \quad (3.22)$$

As mentioned earlier, our goal is to use the orthogonal representation but expressing the Hamiltonian by means of tight-binding parameters. By comparing the terms for a general representation with an orthogonal representation using Eqn. 3.18 and Eqn. 3.19 we get the following relationship

$$\mathbf{h}^{\gamma} = \mathbf{h}^{\alpha} (1 + \mathbf{o}^{\alpha} \mathbf{h}^{\alpha})^{-1}. \quad (3.23)$$

Since this is true for any representation  $\alpha$  it also holds for the tight-binding representation and we can write

$$\mathbf{h}^{\gamma} = \bar{\mathbf{h}} (1 + \bar{\mathbf{o}}\bar{\mathbf{h}})^{-1} \quad (3.24)$$

<sup>2</sup>The different representations can be distinguished in various ways. In this thesis, canonical representations are without superscript, a general representation has the  $\alpha$  superscript, the orthogonal representation has the  $\gamma$  superscript, and the tight-binding representation uses a bar.

and if  $\bar{\mathbf{o}}\bar{\mathbf{h}}$  is small we can expand the inverse in a exponential series and write the Hamiltonian as

$$\mathcal{H}^\nu = \varepsilon_\nu + \bar{\mathbf{h}} - \bar{\mathbf{h}}\bar{\mathbf{o}}\bar{\mathbf{h}} + \bar{\mathbf{h}}\bar{\mathbf{o}}\bar{\mathbf{h}}\bar{\mathbf{o}}\bar{\mathbf{h}} - \dots \quad (3.25)$$

Depending on accuracy, the expansion of the Hamiltonian above can be truncated at a suitable place. For our purposes it is often enough to keep only the first three terms.

### 3.5 The Hamiltonian

By taking a closer look at the augmentation process, the expressions for  $\mathbf{h}^\alpha$  and  $\mathbf{o}^\alpha$  can be identified in order to set up the Hamiltonian and overlap matrices. Using the basis functions expressed in terms of  $|\varphi\rangle$  and  $|\dot{\varphi}\rangle$  (Eqn. 3.18) together with the description of the envelope function in a general representation (Eqn. 3.16), allows us to identify the  $\mathbf{h}^\alpha$  matrix, which can be written as (not showing the indices  $\mathbf{R}L, \mathbf{R}'L'$  and  $\nu$ )

$$h^\alpha = -\frac{\{K, \varphi\}}{\{K, \dot{\varphi}^\alpha\}} + \sqrt{\frac{2}{S}} \{J^\alpha, \varphi\} S^\alpha \{J^\alpha, \varphi\} \sqrt{\frac{2}{S}} \quad (3.26)$$

and furthermore, the diagonal matrix  $\mathbf{o}^\alpha$  is expressed as

$$o^\alpha = -\frac{\{J^\alpha, \dot{\varphi}\}}{\{J^\alpha, \varphi\}} = -\frac{\{J, \dot{\varphi}\} - \{K, \dot{\varphi}\} Q^\alpha}{\{J, \varphi\} - \{K, \varphi\} Q^\alpha}. \quad (3.27)$$

In order to get an abbreviated form of the Hamiltonian we introduce the potential parameters  $C^\alpha$  and  $\Delta^\alpha$  through the relations

$$\begin{cases} C^\alpha = \varepsilon_\nu - \frac{\{K, \varphi\}}{\{K, \dot{\varphi}^\alpha\}} \\ \Delta^\alpha = \frac{2}{w} \{J^\alpha, \varphi\}^2 \end{cases} \quad (3.28)$$

where  $C$  is related to the position of the center of the band and  $\Delta$  is related to the width of the band. For the tight-binding representation, this gives

$$\bar{\mathbf{h}} = \bar{C} - \varepsilon_\nu - \bar{\Delta}^{1/2} \bar{S} \bar{\Delta}^{1/2}, \quad (3.29)$$

where  $\bar{C}$  and  $\bar{\Delta}^{1/2}$  are diagonal matrices.

## 4. The recursion method

The LMTO-ASA basis set, derived in the previous chapter, proves an efficient basis for use in electronic structure calculations. The efficiency comes from a number of factors. The basis set is minimal, using only one basis function per orbital. Furthermore the basis set, at least in the screened, tight-binding, representation is highly localized.

Regardless of the basis set, solving the eigenvalue problem formulated in Eqn. 3.2 by diagonalization causes the computational cost to scale as  $\mathcal{O}(N^3)$  where  $N$  is the number of atoms. Since most bulk materials have translational symmetry,  $N$  can usually be kept to a small number and the cubic scaling is thus seldom a problem for calculations of bulk systems. However, for systems where the periodicity is broken, such as surfaces, defects or embedded clusters, the dimensions of the supercell that are needed to describe the system properly, can grow to sizes where a  $\mathcal{O}(N^3)$  method would be too time consuming. For such systems, other methods of calculating the electronic structure may be better suited. There exists several methods that calculates the electronic properties without solving the actually eigenvalue equation and where the computational cost scales as  $\mathcal{O}(N)$ . An extensive review of  $\mathcal{O}(N)$  methods is given in Ref. [14].

An  $\mathcal{O}(N)$  method that has been used to a large extent in this thesis is the recursion method. The main idea behind this method is to perform, using a recursion formula, a basis change from the original basis to one where the Hamiltonian is tridiagonal, and from that tridiagonal Hamiltonian calculate the local density of states for each atom by using a continued fraction. The recursion method was originally developed for use in solid state physics by Haydock and coworkers [15]. A complete and more formal coverage of the method can be found in Ref. [15], but in the following sections we will outline the main features of the method.

In addition to presenting the recursion method, a brief review of an  $\mathcal{O}(N)$  method based on density matrix purification theory[16], that was used in **Paper I**, can be found in Section 4.7.

### 4.1 The chain model

First we need to show how the Hamiltonian of a quantum mechanical system can be transformed to a tridiagonal (Jacobi) form. Consider a model, as in Fig. 4.1 where an electron has its initial state  $\mathbf{u}_0$  as an orbital on an atom

in a solid. Furthermore, the states  $\mathbf{u}_1$  and  $\mathbf{u}_2$  are states representing a linear combination of orbitals on the atoms that are nearest neighbours and next-nearest neighbours to the atom where  $\mathbf{u}_0$  is located. The electron at  $\mathbf{u}_0$  can

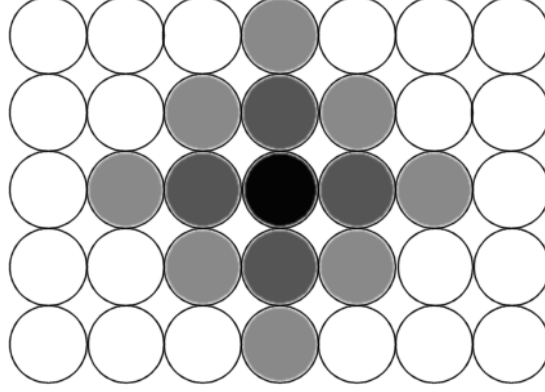


Figure 4.1: Schematic picture of states expanding in space around the central atom. Here the initial state  $\mathbf{u}_0$  is the black circle in the middle, surrounded by the state  $\mathbf{u}_1$  (dark gray) and  $\mathbf{u}_2$  (light gray)

hop to  $\mathbf{u}_1$ , whereas when the electron is in  $\mathbf{u}_1$ , it can hop to either  $\mathbf{u}_0$  or  $\mathbf{u}_2$ . This corresponds to a chain model such as in Fig. 4.2.

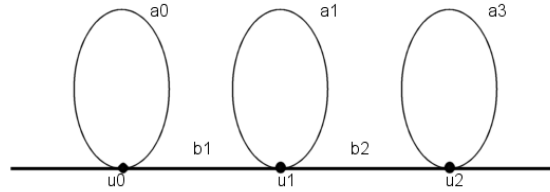


Figure 4.2: The recursion procedure produces an one-dimensional chain model. The set  $\{a_n\}$  corresponds to the on-site energies while the  $\{b_n\}$  set describes the hopping between states.

If we take  $\mathbf{u}_0, \mathbf{u}_1, \mathbf{u}_2, \dots, \mathbf{u}_N$  as orthogonal states, so that an electron positioned on state  $\mathbf{u}_0$  can only hop to the nearest state  $\mathbf{u}_1$ , while electrons in the middle of the chain, say  $\mathbf{u}_n$  can hop to itself or to the neighbouring states  $\mathbf{u}_{n-1}$  and  $\mathbf{u}_{n+1}$ . If we then have the sets of parameters  $\{a_0, a_1, \dots, a_N\}$  for describing the on-site energy and  $\{b_1, b_2, \dots, b_N\}$  for describing the hopping parameters between states, then these sets of parameters describe the action of the Hamiltonian,  $\mathbf{H}$ , on the states by the following recursion relation

$$\mathbf{H}\mathbf{u}_n = a_n\mathbf{u}_n + b_{n+1}\mathbf{u}_{n+1} + b_{n-1}\mathbf{u}_{n-1}. \quad (4.1)$$

This recursion is symmetric since the component  $\mathbf{u}_{n+1}$  in  $\mathbf{H}\mathbf{u}_n$  is identical to  $\mathbf{u}_n$  in  $\mathbf{H}\mathbf{u}_{n+1}$  which is a consequence of the hermicity of the Hamiltonian. If

we represent the state  $\mathbf{u}_n$  as a column vector where the element  $n$  is one and all other elements are zero, we get the Hamiltonian in the basis of these states, and due to the recursion formula it looks like

$$\mathbf{H} = \begin{bmatrix} a_0 & b_1 & 0 & 0 & \dots \\ b_1 & a_1 & b_2 & 0 & \dots \\ 0 & b_2 & a_2 & b_3 & \dots \\ 0 & 0 & b_3 & a_3 & \dots \\ \vdots & \vdots & \vdots & \vdots & \ddots \end{bmatrix}. \quad (4.2)$$

The sets of parameters  $a_n$  and  $b_n$  are called the recursion parameters and are used for constructing the continued fraction that is used for calculating the local density of states for the initial orbital. With the chain model, states lying far from each other can only be reached by hopping through the intermediate states. The consequence of this is that the initial state is mostly influenced by the nearest lying states while the effect from other orbitals, located further away, diminish with the distance to the site of the initial state. The consequence of this is that the chain model gives a localized picture of the orbitals which as we will see further on is a very important feature for treating the system efficiently.

## 4.2 Calculation of the recursion parameters

The parameters  $\{a_0, a_1, \dots\}$  and  $\{b_1, b_2, \dots\}$  can be calculated for an desired orbital in the following way. First, we chose the starting state  $\mathbf{u}_0$  to be the orbital of interest. For example, if want the local density of states of an muffin-tin  $s$  orbital on an atom, we simply take  $\mathbf{u}_0$  to be an  $\varphi_s$  orbital localized on that atom. As previously done, the states are represented by column vectors, and we also introduce the overlap matrix  $\mathbf{O}$  for relating overlap between states to matrix multiplications. The overlap matrix  $\mathbf{O}$  must be self-adjoint and positive definite in order to represent the hermitian inner product of two states.

The first step is, using the recursion relation for state  $\mathbf{u}_0$ , which is assumed to be normalized for the sake of convenience,

$$\mathbf{H}\mathbf{u}_0 = a_0\mathbf{u}_0 + b_1\mathbf{u}_1, \quad (4.3)$$

where the left hand side is known, and  $a_0$ ,  $b_1$  and  $\mathbf{u}_1$  need to be determined. From Eq. 4.3  $a_0$  can be determined by multiplying with  $\mathbf{u}_0^\dagger$  from the left. Due to the orthonormality of the states,  $\mathbf{u}_0^\dagger b_1 \mathbf{u}_1 = 0$  so that  $a_0$  can be calculated as

$$a_0 = \mathbf{u}_0^\dagger \mathbf{O} \mathbf{H} \mathbf{u}_0. \quad (4.4)$$

The next step is to find  $b_1$  and  $\mathbf{u}_1$  which can be done by subtracting  $a_0\mathbf{u}_0$  from Eqn. 4.3 and using orthonormality once again to extract  $b_1^2$  as

$$b_1^2 = [(\mathbf{H} - a_0)\mathbf{u}_0]^\dagger \mathbf{O} [(\mathbf{H} - a_0)\mathbf{u}_0]. \quad (4.5)$$

Since the inner product is positive definite,  $b_1^2$  is greater than zero. By taking  $b_1$  as the positive root of  $b_1^2$ ,  $\mathbf{u}_1$  can be obtained as

$$\mathbf{u}_1 = [(\mathbf{H} - a_0)\mathbf{u}_0]/b_1. \quad (4.6)$$

As seen in Eqn. 4.6,  $\mathbf{u}_1$  is orthogonal to  $\mathbf{u}_0$  and normalized. When these parameters and states are determined the procedure can continue to obtain the parameters for the chain.

A general step of calculating  $\mathbf{u}_{n+1}$ ,  $a_n$  and  $b_{n+1}$  once the preceding parameters are calculated from Eqn. 4.1 is as follows. Similar to the calculation of the first parameters, the orthonormality of the states yields the parameters as

$$a_n = \mathbf{u}_n^\dagger \mathbf{O} \mathbf{H} \mathbf{u}_n, \quad (4.7)$$

$$b_{n+1}^2 = [(\mathbf{H} - a_n)\mathbf{u}_n - b_n\mathbf{u}_{n-1}]^\dagger \mathbf{O} [(\mathbf{H} - a_n)\mathbf{u}_n - b_n\mathbf{u}_{n-1}] \quad (4.8)$$

and

$$\mathbf{u}_{n+1} = [(\mathbf{H} - a_n)\mathbf{u}_n - b_n\mathbf{u}_{n-1}]/b_{n+1}. \quad (4.9)$$

With this procedure, the chain does not terminate until the new state has norm zero. The termination of the chain means that the smallest invariant subset of the initial state has finite dimension. For solid-state systems, the chain does not terminate in general, but continues to infinity. However, as noted previously, states far from the initial state contribute less and less, and in practice, the chain can be terminated even though the final states are finite.

### 4.3 The continued fraction

With the transformation of the Hamiltonian, and the calculation of the sets of the recursion parameters  $\{a_n\}$  and  $\{b_n\}$ , the first part of the problem is solved. What is needed next is to from these parameters calculate the local density of states,  $N(E)$ . This is done by using the properties of Green functions of a finite chain.

A local Green function between two states  $\mathbf{u}$  and  $\mathbf{v}$  has the form of

$$G_{\mathbf{u}\mathbf{v}}(Z) = \mathbf{u}^\dagger \mathbf{O} (Z - \mathbf{H})^{-1} \mathbf{v}, \quad (4.10)$$

where  $Z$  is a complex energy. If the two states are identical, the result is a general diagonal Green function  $G_{00}(Z)$ , which for a state  $\mathbf{u}_0$  is written as

$$G_{00}(Z) = \mathbf{u}_0^\dagger \mathbf{O} (Z - \mathbf{H})^{-1} \mathbf{u}_0. \quad (4.11)$$

The Green function has simple real poles and each pole has a positive residue. The local density of states,  $N(E)$ , for  $\mathbf{u}_0$  is related to the residues of  $G_{00}$  at its singularities. By spectral decomposition of the Green function, it is found that the local density of states is the total density of the eigenvalues weighted

by the squared magnitude of the overlap between each eigenstate and  $\mathbf{u}_0$ . By considering the imaginary part of the Green function closing in on the real axis by letting the complex part of the energy  $i\varepsilon$  go to zero, it is found that

$$N(E) = \lim_{\varepsilon \rightarrow 0} \frac{1}{\pi} \Im[G_{00}(E + i\varepsilon)]. \quad (4.12)$$

Thus, the local density of states can be calculated from the imaginary part of the diagonal Green function. Using the previously obtained results from the chain model, the local Green function corresponding to  $\mathbf{u}_0$  can be calculated from the local Green function (Eqn. 4.11) with the Hamiltonian expressed in the basis of the orthogonal states  $\{\mathbf{u}_n\}$  (Eqn. 4.2) as

$$G_{00}(E) = \left[ \begin{array}{ccccc} E - a_0 & -b_1 & 0 & 0 & \dots \\ -b_1 & E - a_1 & -b_2 & 0 & \dots \\ 0 & -b_2 & E - a_2 & -b_3 & \dots \\ 0 & 0 & -b_3 & E - a_3 & \dots \\ \vdots & \vdots & \vdots & \vdots & \ddots \end{array} \right]_{00}^{-1}. \quad (4.13)$$

An inverse element of a matrix can be written as the ratio of the co-factor<sup>1</sup> of the element to the determinant[17]. Let us define the determinant of the matrix with the first  $n$  rows and columns deleted as  $D_n(E)$  so the determinant of the whole matrix is  $D_0(E)$  and  $D_{n+1}(E)$  is a co-factor of  $D_n(E)$ . With this notation,  $G_{00}$  can be written as

$$G_{00}(E) = \frac{D_1(E)}{D_0(E)} = \frac{1}{D_0(E)/D_1(E)}. \quad (4.14)$$

A Laplacian expansion of the determinant  $D_0(E)$  by its co-factors[18] gives us

$$G_{00}(E) = \frac{1}{E - a_0 - b_1^2 D_2(E)/D_1(E)} \quad (4.15)$$

and by continuing the expansion of the determinants we end up with the continued fraction of

$$G_{00}(E) = \frac{1}{E - a_0 - \frac{b_1^2}{E - a_1 - \frac{b_2^2}{E - a_2 - \frac{b_3^2}{\dots}}}}. \quad (4.16)$$

Since the continued fraction has the same number of  $\{a_n\}$  and  $\{b_n\}$  as the chain model and normally the chain continues into infinity, the fraction has to be terminated in some way in order to be possible to evaluate. Since we want

<sup>1</sup>A co-factor  $C_{ij}$  is the determinant of a matrix with row  $i$  and column  $j$  removed. The sign of the co-factor is depending on  $i$  and  $j$  as  $(-1)^{i+j}$ .

the method to be as efficient as possible while still maintaining the wanted accuracy, it is crucial that the fraction is terminated in a clever way. Just stopping after a given number of recursion steps and terminating the fraction with the latest calculated parameters is usually not enough, so some sort of extrapolation is warranted. If the choice of the terminator is bad, the bands of the orbitals will be falsely described, often with spurious peaks close to the band edges. For metals it is common that the recursion parameter converges for large  $n$  to constant values  $a_\infty$  and  $b_\infty$  and therefore a suitable choice is to extrapolate the calculated parameters to their converged numbers and from these numbers construct the terminator  $t(E)$  as

$$t(E) = \frac{1}{E - a_\infty - \frac{b_\infty^2}{E - a_\infty - \frac{b_\infty^2}{E - a_\infty - \dots}}}. \quad (4.17)$$

Using this terminator  $t(E)$  to terminate the fraction after the already calculated parameters usually gives good results for metals. This particular choice of terminator is called the square-root terminator or the Beer-Pettifor terminator[19]. The converged values  $a_\infty$  and  $b_\infty$  defines the band center and band width. It is worth noting that it is difficult to find suitable terminators for systems with gaps in the bands such as semi-conductors. The recursion parameters for these systems do not converge towards fixed values and the square-root terminator does not manage to describe the band edges and band gaps, so in these cases other ways of terminating the fraction, often combined with analytical methods must be used.

#### 4.4 Self consistency

The recursion method gives, with a well chosen cluster geometry and an accurate number of recursion steps, a good description of the local density of states (LDOS) for the orbitals that the recursion is performed for. But the LDOS in this case is dependent on how the Hamiltonian is set up, and as we know from Eqn. 2.3 and Eqn. 2.4, the Hamiltonian is dependent of the total density of states of the system and therefore also of the LDOS. So in order to get correct results, the recursion algorithm must be combined with a way to update the Hamiltonian and repeat the procedure until self-consistency is obtained.

In our implementation[20, 21], the Hamiltonian and the initial orbitals are defined in the orthogonal LMTO-ASA basis, expressed in tight-binding parameters. This allows us to use the recursion method for obtaining the local density of states for the wanted muffin-tin orbitals, by constructing the Hamiltonian from the potential parameters as

$$H = \varepsilon_v + \bar{h} - \bar{h}\bar{\delta}\bar{h} \quad (4.18)$$

with

$$\bar{h} = \bar{C} - \varepsilon_v + \bar{\Delta}^{1/2}\bar{S}\bar{\Delta}^{1/2}. \quad (4.19)$$

where  $\bar{C}$ ,  $\bar{o}$  and  $\bar{\Delta}$  are potential parameters and  $\bar{S}$  is the structure matrix in the TB-LMTO-ASA representation. As shown in Section 3.5, the potential parameters can be constructed from the Wronskians that ensures smooth matching of the wavefunctions at the muffin-tin radius. It has been showed, that the wavefunctions within the muffin-tin sphere, can be uniquely determined from the occupation of each band ( $s, p$ , and  $d$ ) at the site, the first and second moments  $\mu_{RL}^n$  of the local density of states,  $N_{RL}(\varepsilon)$ , and  $D_l = \phi_{RLV}(r)/\dot{\phi}_{RLV}(r)$ , at the muffin-tin sphere boundary. A self-consistent solution of the LMTO-ASA problem with the recursion method can thus be obtained by, from a starting guess of the potential parameters, constructing the Hamiltonian according to Eqns. 4.18 and 4.19 and calculate the LDOS for each orbital with the recursion method. The LDOS can then be integrated to calculate the zeroth, first and second order moments of the bands where the zeroth order moment corresponds to the occupational number of the orbital. From the moments, the wavefunction inside the muffin-tin spheres can be determined<sup>2</sup> and a new set of potential parameters can be calculated. This process is then repeated until self-consistency is reached.

## 4.5 Non-collinear magnetism

In the previous sections we showed how the recursion method can be used in order to calculate the local density of states for selected orbitals in a system, and we now turn our attention to how the spin polarized density of states can be calculated. According to Eqn. 4.10, the spin polarized density of states  $\mathbf{m}(\varepsilon)$ , shown in Eqn. 2.8, can be expressed as

$$\mathbf{m}(\varepsilon) = -\frac{1}{\pi} \Im \text{Tr}[\boldsymbol{\sigma} G(\varepsilon)], \quad (4.20)$$

where  $G$  is the local Greens function and  $\boldsymbol{\sigma} = \{\sigma_x, \sigma_y, \sigma_z\}$  are the Pauli matrices. In the case of collinear magnetism, a global magnetization axis exists and the magnetic density of states can be calculated as

$$m(\varepsilon) = -\frac{1}{\pi} \Im \text{Tr}[\sigma_z G(\varepsilon)], \quad (4.21)$$

using only diagonal elements of the Green's function which can readily be obtained with the recursion method as outlined in previous sections.

In order to calculate a generalized non-collinear magnetization density, then according to Eqn. 4.20, evaluation of non-diagonal parts of the Green's function is in principle needed. With the use of the recursion method, non-diagonal elements of the Green's function can be calculated either by

<sup>2</sup>Knowledge of the logarithmic derivatives of the wavefunctions,  $D_l = \phi_{RLV}(r)/\dot{\phi}_{RLV}(r)$ , at the sphere boundaries is also needed for constructing the wavefunction, but  $D_l$  can be obtained from the moments of the LDOS and potential parameters from the previous iteration.

performing several recursion procedures, starting from carefully selected linear combinations of muffin-tin orbitals[15, 22] or by performing block recursion calculations[23, 24]. However, the calculation of the off-diagonal parts is computationally more demanding and is avoided in the approach outlined below.

According to Sec.2.4, a local spin quantization axis can be found within each atomic sphere if the magnetization density is approximated so that only interatomic non-collinearity is considered. In principle it should then be possible to rotate the spin density matrix in spin-space so that the local spin axis is diagonal with  $\sigma_z$ . Then the magnetic density of states can be evaluated with Eqn. 4.21 using only diagonal parts of the Green's function. In order to find the angles needed for the rotation of the density matrix, the direction of the local spin axis need to be known. Since this is usually not the case, the spin polarized density of states need to be obtained in a different fashion.

Since  $\sigma_z$  is diagonal,  $m_z(\varepsilon)$  can according to Eqns. 4.20 and 4.21 be obtained using only diagonal elements of the Green's function. If  $\sigma$  can be rotated to  $\sigma'$  so that  $\sigma'_x$  is diagonal, then  $m_x(\varepsilon)$  can also be obtained. Additional rotations to diagonalize  $\sigma'_y$  and obtaining  $m_y(\varepsilon)$  would finally allow us to construct  $\mathbf{m}(\varepsilon)$ . The problem is now to find and perform these rotations.

It can be shown that a rotation in the form of a unitary transformation,  $\mathcal{U}$ , applied to the Hamiltonian,  $H' = \mathcal{U}H\mathcal{U}^\dagger$ , transforms the Green's function in the same way so that  $G' = \mathcal{U}G\mathcal{U}^\dagger$ . Using the unitary property  $\mathcal{U}^\dagger\mathcal{U} = 1$  and the fact that cyclic permutations of matrix multiplications conserve the trace of the product, the generalized magnetic density of states in Eqn. 4.20, can be written as

$$\mathbf{m}(\varepsilon) = -\frac{1}{\pi} \Im \text{tr} \{ \sigma \mathcal{U}^\dagger \mathcal{U} G \mathcal{U}^\dagger \mathcal{U} \} = -\frac{1}{\pi} \Im \text{Tr} [ \sigma' G' ], \quad (4.22)$$

where  $\sigma'$  are the Pauli matrices after the unitary transformation.

Now, by choosing unitary matrices  $\mathcal{U}_1$  and  $\mathcal{U}_2$  which makes  $\sigma'_x$  and  $\sigma'_y$  diagonal we can calculate  $m_x(\varepsilon)$  and  $m_y(\varepsilon)$  through the diagonal elements of  $G$ . These transformations correspond to the spin rotations

$$\sigma'_x = \mathcal{U}_1 \sigma_x \mathcal{U}_1^\dagger = \sigma_z \text{ and } \sigma'_y = \mathcal{U}_2 \sigma_y \mathcal{U}_2^\dagger = \sigma_z. \quad (4.23)$$

A unitary transformation  $\mathcal{U}_3$  for making  $\sigma'_z$  diagonal, which is the identity matrix can also be defined.

The Hamiltonian can be separated into a spin-independent,  $H^0$  and a spin-dependent part  $\mathbf{B}$ , similar as in Eqn. 2.10,

$$H = H^0 \mathbf{1} + \mathbf{B} \cdot \boldsymbol{\sigma}. \quad (4.24)$$

If we now perform a unitary transformation on the Hamiltonian, only the spin-dependent part will be affected, so that

$$H' = H^0 \mathbf{1} + \mathbf{B} \cdot \mathcal{U} \boldsymbol{\sigma} \mathcal{U}^\dagger. \quad (4.25)$$

The matrix elements of the Hamiltonian can now be constructed using LMTO parameters in the most localized representation in the first order approximation of Eqn. 4.18. We index the site and orbitals of the matrix elements with subscript  $Q = RL$  and denote the spin-independent parts of the potential parameters with superscript 0 and the spin-dependent parts with superscript 1<sup>3</sup>. The matrix elements of the spin-independent part  $H^0$  of the Hamiltonian then looks like

$$H_{QQ'}^0 = \bar{C}_Q^0 + \Delta_Q^0{}^{1/2} S_{QQ'}^- \Delta_{Q'}^0{}^{1/2} + \Delta_Q^1{}^{1/2} S_{QQ'}^- \Delta_{Q'}^1{}^{1/2} \mathbf{m}_Q \cdot \mathbf{m}_{Q'} \quad (4.26)$$

and the spin-dependent part can be written as

$$\mathbf{B}_{QQ'} = (\bar{C}_Q^1 + \Delta_Q^1{}^{1/2} \bar{S}_{QQ'}^- \Delta_{Q'}^1{}^{1/2}) \mathbf{m}_Q + \Delta_Q^0{}^{1/2} S_{QQ'}^- \Delta_{Q'}^1{}^{1/2} \mathbf{m}_{Q'} \quad (4.27)$$

$$+ \Delta_Q^1{}^{1/2} S_{QQ'}^- \Delta_{Q'}^1{}^{1/2} \mathbf{m}_Q \times \mathbf{m}_{Q'} \quad (4.28)$$

With the Hamiltonian built up of these matrix elements, the recursion method can now be used three consecutive times, for the unitary transformations  $\mathcal{U}_1$ ,  $\mathcal{U}_2$  and  $\mathcal{U}_3$  in order to obtain  $m_x(\varepsilon)$ ,  $m_y(\varepsilon)$ , and  $m_z(\varepsilon)$ . By integrating the components of the spin polarized DOS up to the Fermi energy, the direction of the local spin axis can then be obtained.

## 4.6 Spin-orbit coupling

In order to take relativistic effects into account then, according to Eqn. 2.11, a spin-orbit coupling term can be added the Hamiltonian so that

$$H = H_{sr} + H_{SO}, \quad (4.29)$$

where  $H_{sr}$  is the scalar relativistic part of the Hamiltonian and  $H_{SO}$  includes the spin-orbit coupling  $\xi \mathbf{L} \cdot \mathbf{S}$ , and may also include an orbital polarization correction term according to Eqn. 2.13. In the case of a collinear magnetization density,  $H_{sr}$  is given by the LMTO-ASA Hamiltonian defined in Eqn. 3.25 and the addition of the  $H_{SO}$  term makes no difference for the procedure of the recursion method, except that the spin-up and spin-down parts of the Hamiltonian are no longer decoupled from each other.

The inclusion of the  $H_{SO}$  term is not restricted to collinear magnetization densities, and if non-collinear magnetization densities are considered, then  $H_{SO}$  is added to the Hamiltonian in Eqn. 4.25. Since  $H_{SO}$  is spin dependent, the rotation  $U$  operates on  $H_{SO}$  resulting in

$$H' = H^0 \mathbf{1} + \mathbf{B} \cdot U \boldsymbol{\sigma} U^\dagger + U H_{SO} U^\dagger. \quad (4.30)$$

According to the procedure in the previous section,  $U$  can then be varied in order to obtain the magnetization density in the three orthogonal directions

<sup>3</sup>As an example,  $\bar{\Delta}^0 = (\bar{\Delta}^\uparrow + \bar{\Delta}^\downarrow)/2$  and  $\bar{\Delta}^1 = (\bar{\Delta}^\uparrow - \bar{\Delta}^\downarrow)/2$

needed. Compared to the scalar relativistic treatment, the rotation operator  $U$  corresponds to a rotation in real space as well as in spin-space, compared to  $\mathcal{U}$  that only need to rotate in spin-space. The real space rotation with  $U$  is performed in order to obtain orbital moments and related anisotropy energies.

## 4.7 O(N) with Density Matrix Purification

One of the few limitations of the recursion method is the difficulty to construct continued fraction terminators that can treat band gaps well, and the method is thus in practice limited to metals. This is a peculiar fact since most  $\mathcal{O}(N)$  methods only work for materials that have a band-gap. One class of  $\mathcal{O}(N)$  methods that need a gap is based on density matrix purification[16]. The basic idea behind density matrix purification theory is that the single-particle density matrix,  $P$  can be obtained as

$$P = \theta(\mu I - H) = \lim_{n \rightarrow \infty} F_n(F_{n-1}(\dots F_0(H)\dots)), \quad (4.31)$$

where  $I$  is the identity matrix and  $\theta$  is the Heaviside step function, which projects all  $N_{\text{occ}}$  eigenvalues of the occupied states of the Hamiltonian  $H$  to 1 and all eigenvalues of the unoccupied states above the chemical potential  $\mu$  to 0. In  $F_0(H)$  the eigenvalue spectrum of  $H$  is rescaled to the interval of convergence, typically  $[0, 1]$ , in reverse order with the highest (unoccupied) eigenvalue close to 0 and the lowest (occupied) eigenstate close to 1. The polynomials  $F_n$  in Eqn. (4.31) gradually shift the eigenvalues toward 0 for the unoccupied states and toward 1 for the occupied states, resulting in a more “purified” approximation of the density matrix for each iteration.

At convergence, the density matrix given by Eqn. (4.31) fulfill

$$\begin{aligned} \text{Tr}(P) &= N_{\text{occ}}, \\ P^2 &= P, \\ [P, H] &= PH - HP = 0, \end{aligned} \quad (4.32)$$

where  $N_{\text{occ}}$  is the number of occupied states. If a localized basis set is used, the density matrix can become sparse for non-metallic system due to the exponential radial decay of the Wannier functions. The  $\mathcal{O}(N)$  behaviour comes from the fact that the purification steps can be performed by using only matrix-matrix multiplications, for which the computational cost scales linearly with system size if the matrices are sparse.

There exist a wide variety of purifications schemes, and in **Paper I** we present an implementation of two density matrix purification methods using a LMTO-ASA basis set. The two schemes that have been implemented is the second order trace correcting scheme and the fourth order trace resetting scheme. A brief discussion of these two schemes follows below and more details regarding these methods can be found in Refs. [25] and [26].

### 4.7.1 Trace correcting purification

The McWeeny purification requires knowledge of the chemical potential, which in general is unknown. This problem can be solved by an adaptive guessing procedure, but that would increase the computational cost. With the trace correcting schemes, the number of occupied states,  $N_{occ}$  is enough, and the chemical potential is thus not needed. In the 2<sup>nd</sup>-order trace correcting purification scheme (TC2) with the operators expressed in an orthogonal representation, the density matrix  $P^{(0)}$  is given by

$$X_1 = F_0(H) = \frac{\epsilon_{\max} I - H}{\epsilon_{\max} - \epsilon_{\min}}, \quad (4.33)$$

$$X_{n+1} = F_n(X_n) = X_n + \sigma_n (I - X_n) X_n, \quad (4.34)$$

$$P = \lim_{n \rightarrow \infty} X_n. \quad (4.35)$$

The trace correcting sign factor,  $\sigma_n = \pm 1$ , is chosen to minimize the occupation error in the updated approximation,  $\Delta N_{n+1} = |N_{occ} - \text{Tr}(X_{n+1})|$ . The constants  $\epsilon_{\max}$  and  $\epsilon_{\min}$  are upper and lower estimates of the highest and lowest eigenvalues of  $H$ . Using these spectral bounds,  $H$  is normalized to  $X_1$ , with all its eigenvalues in reverse order, rescaled and shifted to the interval  $[0, 1]$ . The change in the occupation between two iterations, i.e., the trace correction, can be used to estimate the idempotency convergence since

$$|\text{Tr}(X_{n+1}) - \text{Tr}(X_n)| = |\text{Tr}[(I - X_n)X_n]|, \quad (4.36)$$

which vanish at idempotency when  $X_n = (X_n)^2$ .

### 4.7.2 Trace resetting purification

In the case of degeneracy and fractional occupation the density matrix is not idempotent, i.e. the eigenvalues of the degenerate states are not fully occupied or non-occupied. Trace correcting purification does not work for these problems. Instead, a hybrid trace resetting purification scheme can be used

which can be explained by the following algorithm

$$\begin{aligned}
& X_1 = (\epsilon_{\max} I - H) / (\epsilon_{\max} - \epsilon_{\min}) \\
& \text{while } Error > ErrorLimit \\
& \quad \gamma_n = (N_{\text{occ}} - \text{Tr}[f(X_n)]) / \text{Tr}[g(X_n)] \\
& \quad \text{if } \gamma_n > 6 \\
& \quad \quad X_{n+1} = 2X_n - X_n^2 \\
& \quad \text{else if } \gamma_n < 0 \\
& \quad \quad X_{n+1} = X_n^2 \\
& \quad \text{else} \\
& \quad \quad X_{n+1} = 4X_n^3 - 3X_n^4 + \gamma_n X_n^2 (I - X_n)^2 \\
& \quad \text{end} \\
& \quad \text{estimate } Error \\
& \text{end while} \\
& P = X_{n+1}
\end{aligned} \tag{4.37}$$

In trace resetting purification a fourth order purification polynomial is used, if  $\gamma_n \in [0, 6]$ , to expand the step function and force the trace to be correct after each iteration. If  $\gamma_n$  is outside of the interval, the trace resetting may project eigenvalues out of the range of convergence and instead the second order trace correcting scheme is used. The trace-resetting scheme requires no knowledge of the chemical potentials or the band-gap, it performs well both for high and low occupation, and the scheme converges to the correct occupation both in the case of degeneracy and fractional occupation.

### 4.7.3 LMTO self-consistency

As was discussed in Sec. 4.4, the electron density and the potential inside a muffin-tin sphere and the corresponding potential parameters can be uniquely determined[27] from the occupation of each band ( $s, p$ , and  $d$ ) at the site, the first and second moments  $\mu_{RL}^n$  of the local density of states,  $N_{RL}(\epsilon)$ , and the logarithmic derivative  $D_l = \varphi_{RLV}(r) / \dot{\varphi}_{RLV}(r)$ , at the sphere boundary.

Since we are working with nearly energy independent density matrices, the local density of states is not readily obtained in an explicit form. However, the local density of states can be written as

$$\mathcal{N}_{RL}(\epsilon) = \sum_i |\langle \varphi_{RL} | \psi_i \rangle|^2 \delta(\epsilon - \epsilon_i), \tag{4.38}$$

which can be used to evaluate the moment  $\mu^n$  of order  $n$  as

$$\begin{aligned}
\mu_{RL}^n &= \int \epsilon^n \mathcal{N}_{RL}(\epsilon) d\epsilon = \\
\langle \varphi_{RL} | H^n | \varphi_{RL} \rangle &= \text{Tr}_{RL} [PH^n].
\end{aligned} \tag{4.39}$$

Once the density matrix  $P$  is obtained, all moments of order  $n$  is thus obtained by taking the trace of the product of  $P$  and  $H^n$ . The logarithmic derivative can be determined from the calculated moments and the potential parameters.

From the obtained moments and the logarithmic derivatives, the charge density inside the muffin-tin spheres can be calculated and new potential parameters and a new Hamiltonian can be obtained. This procedure can then be iterated until self-consistency is achieved.



## 5. Magnetic ordering

The magnetic configuration of a single isolated atom can be determined with the use of Hund's rules. When atoms form solids, their magnetic behaviour is however not as predictable due to the competitions between the exchange interactions which favor the magnetization of magnetic moments and the tendency of electrons to hop from atom to atom in the material. If the exchange interactions in the solid are weak, the solid will lack a global magnetic ordering even though the constituting atoms have a finite moment in their atomic configuration. More pronounced interactions may result in one of a variety of magnetic orderings, such as these illustrated in Fig. 5.1

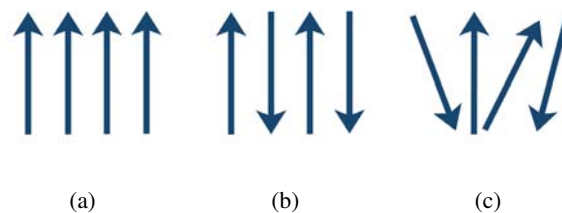


*Figure 5.1:* Examples of magnetic orderings. From left to right, the magnetic order is ferromagnetic, antiferromagnetic, and non-collinear.

Magnetic orderings where there exists a global magnetization axis along which the spins align either parallel (ferromagnetic) or antiparallel (antiferromagnetic) to each other, as depicted in the first two panels of Fig. 5.1, are the most common orderings. If no global magnetization axis is present, the magnetic ordering is non-collinear. While the cause of ferro- and antiferromagnetic ordering can often be predicted and described with the use of well established theories, the origins of non-collinear ordering are usually not as well understood. In Chapters 7 and 8 of this thesis, different causes for non-collinear magnetic orderings will be discussed in detail. We will however precede these results by reviewing the theories considering the origin of ferromagnetic and antiferromagnetic ordering.

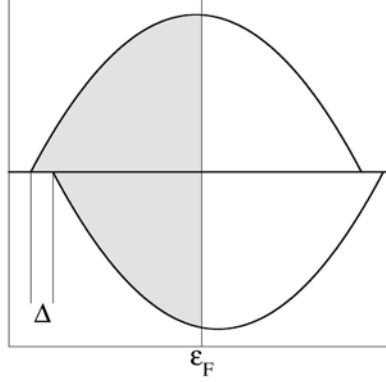


Figure 5.2: Schematic view of itinerant electron bands spin-split by a factor  $\Delta$ .

## 5.1 The Stoner criterion

Stoner theory describes the competition between the kinetic energy and the exchange energy for a system of itinerant electrons. A detailed derivation of the Stoner criterion can be found in many textbooks, i.e. Refs. [5] and [28].

Consider an itinerant system with almost free electrons moving in a crystal field, resulting in a continuous density of states,  $N(\varepsilon)$ . The stability of the non-magnetic state can be probed by introducing a magnetization in the system by moving electrons from one spin channel to the other. The magnetization,  $m$  causes a splitting  $\Delta$ , between the two different spin bands, which can be seen in Fig. 5.2. In Stoner theory, the splitting  $\Delta$  depend on the effective, or Stoner, exchange interaction  $I$  so that,  $\Delta = Im$ . The spin dependent density of states  $N^\sigma(\varepsilon)$  can be expressed as the non-magnetic DOS  $N^0(\varepsilon)$  shifted by  $\Delta/2$  so that

$$N^\uparrow(\varepsilon) = N^0\left(\varepsilon + \frac{Im}{2}\right), \quad N^\downarrow(\varepsilon) = N^0\left(\varepsilon - \frac{Im}{2}\right). \quad (5.1)$$

Since the number of occupied electrons  $N_{occ}$  is calculated by taking the sum of the spin dependent density of states and integrating to the Fermi level  $\varepsilon_F$ , and the moment  $m$  is obtained by integrating the difference of the spin dependent density of states to  $\varepsilon_F$ , two equations for determining  $\varepsilon_F$  and  $m$  can be constructed as  $m = F(m)$  with

$$F(m) = \int^{\varepsilon_F(m)} \left[ N^0\left(\varepsilon + \frac{Im}{2}\right) - N^0\left(\varepsilon - \frac{Im}{2}\right) \right] d\varepsilon, \quad (5.2)$$

which need to be solved self-consistently.

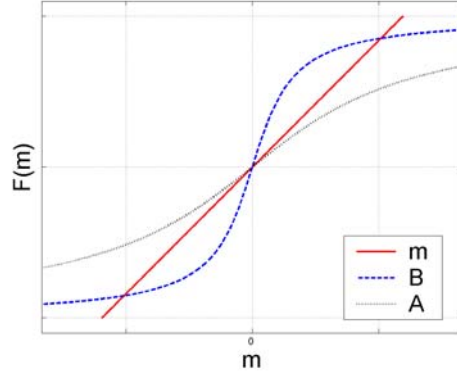


Figure 5.3: Graphical solutions for  $F(m) = m$  for the Stoner model. Function A has only a non-magnetic solution while function B has two magnetic solutions as well as a non-magnetic solution.

From Fig.5.2, we see that for a sufficiently large splitting  $\Delta$ , the moment  $m$  will be saturated with a value  $m^\infty$  corresponding to a total spin polarisation. Until the moment saturizes,  $F(m)$  will increase with increasing splitting i.e.  $F'(m) \geq 0$ . From these observations, we can sketch two possible functions  $F(m)$ , which are shown in Fig. 5.3. The function denoted by A has only the trivial non-magnetic solution  $m = 0$  while the function B has three possible solutions,  $m = \pm m_S$  and  $m = 0$ . This non-magnetic solution is however unstable. The derivative  $F'(m)$  can be obtained from Eqn. 5.2 as

$$F'(m) = \frac{I}{2} \left[ N^0 \left( \epsilon_F + \frac{Im}{2} \right) + N^0 \left( \epsilon_F - \frac{Im}{2} \right) \right] + \left[ N^0 \left( \epsilon_F + \frac{Im}{2} \right) - N^0 \left( \epsilon_F - \frac{Im}{2} \right) \right] \frac{d\epsilon_F}{dm}. \quad (5.3)$$

For  $m = 0$ , Eqn. 5.3 reduces to  $F'(0) = IN^0(\epsilon_F)$ . From Fig. 5.3 we see that a sufficient condition for a ferromagnetic solution is  $F'(0) > 1$ , which gives the Stoner criterion

$$IN^0(\epsilon_F) > 1. \quad (5.4)$$

The Stoner factor  $I$  is a material specific property and can be calculated using density functional theory.

According to Stoner theory, a transition to a ferromagnetic phase can thus be obtained when the non-magnetic phase exhibits a large density of states at the Fermi level. This is the reason for the occurrence of ferromagnetism among the elements in the late 3d series, (Fe, Co, and Ni), where the spatially localized wave-functions of the 3d electrons cause a high density of states at the Fermi level and a rather large value of  $I$ .

A ferromagnetic state can for certain conditions be unstable towards anti-ferromagnetic ordering. That means that the energy can be lowered by form-

ing two sublattices, where the magnetization  $m$  have different directions for each of the sublattices. The antiferromagnetic ordering can occur if the antiferromagnetic susceptibility  $\chi_{AFM}$  is larger than the ferromagnetic counterpart  $\chi_{FM}$ . It can be shown, using Heines[29] crossing theorem with a moments expansion of the susceptibilities[30], that the quantity  $\chi_{AFM} - \chi_{FM}$  changes sign twice as a function of the band-filling. As a result of these crossings, compounds with half-filled bands are more prone towards antiferromagnetic ordering, while materials with low or high band-filling prefer to order ferromagnetically. This explains why Cr and Mn tend to form antiferromagnetic compounds.

Antiferromagnetic ordering can also be analyzed in terms of the  $\mathbf{q}$ -dependent susceptibility  $\chi(\mathbf{q})$ , which will be discussed in the following section.

## 5.2 Magnetic susceptibility and nesting

The enhanced uniform susceptibility  $\chi$ , can be generalized to treat the response of a nonuniform magnetic field[5] characterized by the wave vector  $\mathbf{q}$ , resulting in  $\chi = \chi(\mathbf{q})$ . The unenhanced susceptibility  $\chi_0(\mathbf{q})$  describes the instantly induced magnetization density,  $\Delta m$ , due to a small applied magnetic field,  $\Delta B$  so that  $\Delta m(\mathbf{q}) = \chi_0(\mathbf{q})\Delta B(\mathbf{q})$ . If a small field is applied, a small magnetization density will thus be induced. This change in magnetization density will affect the exchange-correlation potential for the system, which will result in an effective increase in the applied field, governed by the Stoner factor  $I(\mathbf{q})$

$$\Delta m(\mathbf{q}) = \chi_0(\mathbf{q})(\Delta B(\mathbf{q}) + I(\mathbf{q})\Delta m(\mathbf{q})). \quad (5.5)$$

The self-consistent response can then be written as  $\Delta m(\mathbf{q}) = \chi(\mathbf{q})\Delta B(\mathbf{q})$ , which combined with Eqn. 5.5 gives us an expression for the enhanced susceptibility

$$\chi(\mathbf{q}) = \frac{\chi_0(\mathbf{q})}{1 - I(\mathbf{q})\chi_0(\mathbf{q})}. \quad (5.6)$$

An analytical expression of the unenhanced susceptibility can be obtained by using perturbation theory on the response in a nearly-free electron limit. The resulting expression can be written using the Lindhard formula[31]

$$\chi_0(\mathbf{q}) = -\frac{1}{\Omega} \sum_{\nu\mu} \int \frac{f(\epsilon_{\mathbf{k}\nu})[1 - f(\epsilon_{\mathbf{k}-\mathbf{q}\mu})]}{\epsilon_{\mathbf{k}-\mathbf{q}\mu} - \epsilon_{\mathbf{k}\nu}} d\mathbf{k}, \quad (5.7)$$

where the integration is performed over the first Brillouin zone,  $f(\epsilon)$  is the Fermi function and  $\epsilon_{\mathbf{k}\nu}$  is the eigenvalue for band  $\nu$  at  $\mathbf{k}$ . By examining Eqn. 5.7 we see that the denominator becomes small when the ordering vector connects  $\mathbf{k}$ -points with nearly equal eigenvalues. Furthermore, we see that at very low temperatures, the Fermi functions approaches step functions, and

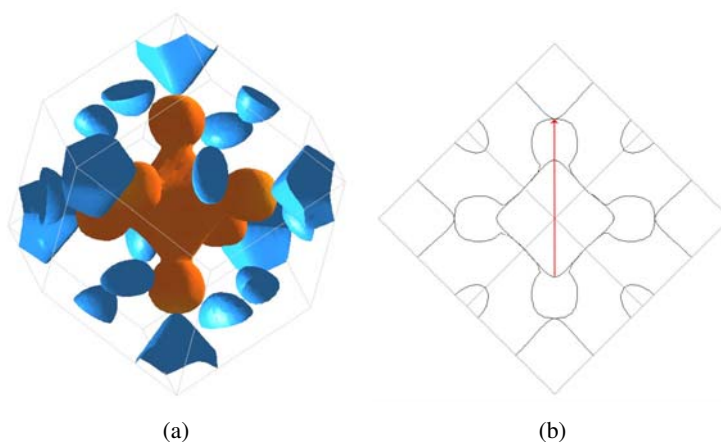


Figure 5.4: The Fermi surface of Cr (left) and a cut of the Fermi surface(right).

the only ordering vectors contributing to the susceptibility are those that connects an empty state to an occupied state on the Fermi surface. As a result, the unenhanced susceptibility grows very large for an ordering vector  $\mathbf{q}$ , that connects planar sections of one or more Fermi surfaces. The concept of having two Fermi surfaces that can coincide for a rigid shift along a vector  $\mathbf{q}$ , is called *nesting*, and the vector  $\mathbf{q}$  is then a nesting vector.

In order to illustrate the effect of a nesting vector we can consider the Fermi surface for bcc Cr, displayed in Fig. 5.4(a). The tetrahedron shaped surface in the center of the Brillouin zone is an electron surface, while the tetrahedrons centered at the  $H$  corners of the Brillouin zone are hole pockets. Due to the spherical shaped surfaces at the corners of the electron tetrahedron, it is difficult to observe any obvious nesting vectors. However, if we plot a cut of the Fermi surfaces and neglect everything except the tetrahedrons, which is done in Fig. 5.4(b) we can find a nesting vector along the  $Z$  direction with a length of approximately half a reciprocal lattice vector. A nesting vector that is exactly half a reciprocal lattice vector would cause a magnetic ordering with ferromagnetic planes where the magnetization direction alternates between up and down along the nesting vector. This behaviour would divide the lattice into two sub-lattices with different magnetization directions, which is the definition of an antiferromagnet. The nesting vector for Cr is in fact not exactly a half lattice vector but corresponds to an ordering vector of  $\mathbf{q} = (2\pi/a)(0, 0, 0.952)$ . As a result, Cr forms not an ordinary antiferromagnet, but an incommensurate spin density wave.[32]

### 5.3 Exchange interactions

For complex magnetic structures, the magnetic ordering can not always be determined from the  $\mathbf{q}$ -dependent susceptibility. For such systems it can be useful to model the magnetic structure within the classical Heisenberg model[31], where the Hamiltonian can be expressed as

$$H = - \sum_{i \neq j} J_{ij} \hat{\mathbf{s}}_i \cdot \hat{\mathbf{s}}_j, \quad (5.8)$$

where  $J_{ij}$  is the effective exchange interaction between the localized spins  $\mathbf{s}_i$  and  $\mathbf{s}_j$ . The Heisenberg model is by definition well suited for systems where the magnetic moments are localized, and in these cases it is often enough to only take nearest-neighbour interactions into account. For more itinerant systems, the Heisenberg model can work as well, but then the range for which  $J_{ij} \neq 0$  need to be increased. With a correct set of  $J_{ij}$ , the Heisenberg model can be used to study ground state configurations as well as the magnetic behaviour at finite temperatures.

The exchange interactions  $J_{ij}$  in Eqn. 5.8 can be obtained in reciprocal space by the frozen magnon method[33, 34] or directly in real space by using the Liechtenstein-Katsnelson formula where the energy change related to an infinitesimal rotation is calculated by means of the local force theorem[35, 36]. Within the RS-LMTO-ASA method,  $J_{ij}$  can be calculated as

$$J_{ij} = \Im \frac{\text{Tr}}{4\pi} \int_{-\infty}^{\epsilon_F} \delta_i(\epsilon) G_{ij}^{\uparrow\uparrow} \delta_j(\epsilon) G_{ji}^{\downarrow\downarrow} d\epsilon, \quad (5.9)$$

where the trace is over orbital indices,  $G_{ij}^{\sigma\sigma}$  is the propagator for spin  $\sigma$  between sites  $i$  and  $j$ , and  $\delta_i$  is a diagonal matrix whose elements are

$$\delta_{li}(\epsilon) = \frac{C_{li}^{\downarrow} \Delta_{li}^{\uparrow} - C_{li}^{\uparrow} \Delta_{li}^{\downarrow} + (\Delta_{li}^{\downarrow} - \Delta_{li}^{\uparrow}) \epsilon}{(\Delta_{li}^{\uparrow} \Delta_{li}^{\downarrow})^{\frac{1}{2}}}, \quad (5.10)$$

where  $l$  is an orbital index,  $C_{li}^{\sigma}$  and  $\Delta_{li}^{\sigma}$  are potential parameters in the orthogonal LMTO-ASA representation. If  $\Delta_{li}^{\uparrow} = \Delta_{li}^{\downarrow}$ , Eqn. 5.10 becomes energy independent with  $\delta_i$  corresponding to the difference between the center of the spin-up and spin-down bands.

### 5.4 Interlayer exchange coupling

The Heisenberg Hamiltonian works best for spins close to each other. An almost opposite situation is two magnetic atoms far from each other which are separated by nonmagnetic atoms. The mechanism for exchange interactions in this situation is an indirect interaction between the localized moments through the conduction electrons of the non-magnetic material. These interactions are described by the RKKY theory[37–39] and can not only describe interactions

between isolated atoms but also between magnetic layers separated by a non-magnetic spacer. The exchange interactions between such layers are quantified by the interlayer exchange coupling,  $J_{IEC} = E_{AFM} - E_{FM}$ , i.e. the energy needed to switch the magnetization direction for one of the layers.

For large separations, the exchange coupling can be written as[40, 41]

$$J_{IEC} = E_{AFM} - E_{FM} = - \sum_{\alpha} \frac{J_{\alpha}}{N^2} \sin(q_{\perp}^{\alpha} N + \phi_{\alpha}) \quad (5.11)$$

where  $N$  is the spacer thickness and where the sum is over critical spanning vectors  $q_{\perp}^{\alpha}$  of the bulk Fermi surface of the spacer material. The amplitude  $J_{\alpha}$  of the coupling period  $\alpha$  depends on the spin-asymmetry of the reflection coefficients at the interfaces. It also depends on the Fermi velocity and the curvature of the Fermi surface at the Fermi surface points spanned by  $q_{\perp}^{\alpha}$ . The phase of the coupling,  $\phi_{\alpha}$ , depends on both the reflection coefficients and on the Fermi surface topology. Hence the coupling is characterized by a set of superimposed oscillations where the periods are given by the extremal Fermi surface calipers.

The IEC oscillates as function of the spacer layer thickness and the period can be obtained straight forward from total energy calculations or by analysing the calipers of the Fermi surface. The IEC for Fe layers separated by a  $\text{Cu}_x\text{Pd}_{1-x}$  alloy was studied in **Paper II** where the shape of the Fermi surface and accordingly the oscillating period of the IEC changed with the degree of alloying. In **Paper III** we study the effect of the IEC for Fe layers with a V spacer when magnetic impurities are introduced in the spacer.



## 6. High moment materials

In addition to the exciting aspects of fundamental physics, research on magnetic materials is often motivated by possible use in applications for data storage. The fundamental principle for magnetic data storage is that the information is decomposed into binary units (bits) where each bit is stored as the magnetization direction of small regions of a magnetic media. Since there is an evergrowing need for increased data storage capacity, these bits need to be stored as close as possible i.e. the areal density need to be increased.

### 6.1 Material prerequisites for data storage

There are three parts of a magnetic storage device that can be identified as having a critical importance for the storage density. The read head, the device that reads the information from the magnetic media, needs to have a very high sensitivity as well as a high signal-to-noise ratio in order to sense the magnetic information stored on each bit. Typically the read head is a magnetic sensor built up by a sandwich of magnetic and nonmagnetic layers. The sensor can use either the giant magnetoresistivity effect[42](GMR) which is caused by spin-dependent scattering of conduction electrons in magnetically coupled layers separated by a non-magnetic metallic layer, or in newer devices the tunneling magnetoresistivity effect[43](TMR) where it is the spin-dependent tunneling through an isolator situated between magnetic layers that cause the magnetoresistivity.

The recording media need to fulfill several material properties since it must allow for information to be written to the media at a high speed and the stored information must be kept unchanged for long times. As the volume of the magnetic bits decrease, so do the magnetic field emitted from a bit. A large saturation magnetization of the magnetic media is then important in order to ensure a readable field from the bits. Due to the decreased volume, the bits do also become more sensitive to thermal fluctuations. In order to keep the recording media stable against thermal fluctuations, and withstand interactions from neighbouring bits, the magnetic media need to exhibit a high magneto-crystalline anisotropy energy(MAE)

The write head, which writes the information to the magnetic media, need to be able to produce a magnetic field strong enough to flip the magnetic directions in the bits, and localized enough to not affect surrounding bits. If the MAE of the bits increase, the field from the write head need to increase

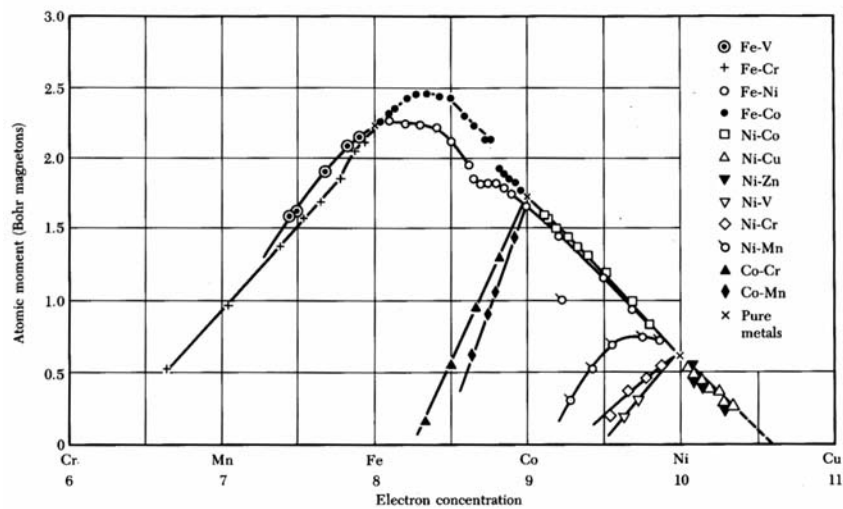


Figure 6.1: The Slater-Pauling curve which shows the magnetic moment per atom as a function of electron concentration for transition metal alloys.

as well. Due to the increased bit density the area of the read head must be kept small and the only remaining way of increasing the write field is to increase the magnetization saturation density of the material in the write head. As the name indicates, the saturation magnetization density of a material is determined by its magnetic moment and its density.

In this chapter, we will focus on high moment materials for use in magnetic write heads. The materials considered are based on alloys of Fe and Co, where not only the chemical composition but also the geometrical configuration of the Fe-Co based materials are varied.

## 6.2 Bulk Fe-Co alloys

The Slater-Pauling curve, displayed in Fig. 6.1 shows the average magnetic moment for different transition metal compounds as a function of the number of valence electrons. The maximum of the Slater-Pauling curve occurs not for a pure element, but for an Fe-Co alloy with a concentration of approximately 35% Co. This is also the composition for which the largest known saturation magnetization density, of  $\sim 2.45$  T, is obtained.<sup>1</sup>

Bulk Fe-Co alloys have been the subject of several studies, experimental[44–46] as well as theoretical[47–49], and it has been shown that the non-linear behaviour of the average magnetic moment is caused by

<sup>1</sup>Larger magnetic moments per atom can be found for certain rare-earth elements i.e. Gd which has a spin moment of  $7\mu_B$ , but Gd has a low critical temperature and is thus not ferromagnetic at room temperature.

increased spin moments of the Fe atoms while the magnetic moment of the Co atoms stays constant. According to these studies, the moment of the Fe atoms increases from  $2.2 \mu_B$  for pure Fe to up to  $3.0 \mu_B$  for Co concentrations higher than 50%. The behaviour of the moments for both Fe and Co atoms can be explained by considering their density of states. In a rigid band picture, the common explanation of the magnetization behaviour is that for the Fe rich side, the Fermi level is pinned to a minimum in the density of states of the minority spin. Since the majority band of Fe is not filled and the minority band is in a minimum, an upward shift of the Fermi level, corresponding to increasing the number of electrons, increases the number of majority spins more than the minority spins and thus the magnetic moment increases. On the Co rich side, the magnetization depends on the number of available  $d$  holes since the majority band is full. This implies that when the Fermi level is shifted down, electrons disappear from the minority band while the number of electrons in the majority band is kept almost constant. These two effects intersect at  $\sim 35\%$  Co content and produce the maximum on the magnetization curve. However, due to the limited charge transfer present between Fe and Co atoms in Fe-Co alloys, which is usually less than 0.1 electron per atom, the rigid band picture can not single handed account for the whole enhancement of the Fe spin moments. It is actually so, as will be shown in later sections, that a proper explanation of the enhanced Fe moments also need to include hybridization effects of the Fe bands due to interactions with surrounding Co atoms. Fully relativistic calculations on Fe-Co alloys[50] show that the orbital moments do not follow the trend that the spin moments have, but instead increases monotonically with increasing Co concentration. According to these results, the orbital moments of the alloys lie between  $0.06 \mu_B$  and  $0.12 \mu_B$  per atom.

With the knowledge of the magnetic behaviour of bulk Fe-Co alloys, the question arises: How can the magnetic moment for such systems be tuned to overcome the bulk limit of  $2.45 \mu_B$  per atom? The two most apparent approaches are to either change the chemical composition by alloying Fe-Co system with other elements, or to change the structure of the material.

### 6.3 Artificial structures

One possibility to tailor the magnetic properties of a material is to grow multilayers out of it. A multilayer is usually grown by sequentially depositing different elements onto a substrate. If the depositing rate of the used elements is well known, the chemical composition and the number of interfaces can be controlled by varying the exposing times of the substrate. Multilayers do not only offer a good possibility to control the stoichiometric composition of the compound, but they can also be used to stabilize crystalline phases of materials that are unstable in bulk. One important example is Co that can be

stabilized in the bcc structure[51] despite the fact that the equilibrium crystal structure of bulk Co is hcp.

In addition to growing multilayers, materials with tailored composition can also be built with clusters as building blocks. Clusters can be created from a gas aggregation source, size selected, and deposited on a surface of choice[52]. The clusters can also be covered by another compound by simultaneously using a ordinary sputtering device in addition to the cluster source. The combination of size selection and embedding offer large possibilities to control the composition of the deposited material. As in the case of multilayers it is, however, difficult to control the interdiffusion between the clusters and the embedding matrix. The structure of the deposited clusters can also be difficult to regulate. Compared to multilayers that in the ideal case have interfaces only in one dimension, clusters can have a larger surface to volume ratio depending on the radius of the cluster.

## 6.4 Multilayers

There exist a number of experimental studies of Fe-Co multilayers and even though a concentration behaviour of the magnetic moments resemble the Slater-Pauling curve for most of the studies, the results and conclusions of these studies show a significant spread. The variation between different experimental findings have inspired several theoretical studies which are reported in Papers **IV, V, and VI**.

### 6.4.1 Magnetic moments

Based on the analogy with bulk alloys, the average spin moments of multilayers consisting of Fe and Co should have an non-linear behaviour as a function of the concentration. In Fig. 6.2 a calculated average magnetic moments for a selection of Fe-Co multilayers is shown, and as expected a Slater-Pauling like behaviour is found; however, the maximum of the moment curve seems to be slightly shifted towards a higher Fe concentration. The concentration dependent behaviour can be seen in more detail in Fig. 6.2 where calculated average magnetic moments for multilayers with a combined thickness corresponding to 8 monolayers, as a function of the Co concentration is shown. A slight enhancement of the magnetic moment compared to pure Fe is found for the  $\text{Fe}_7\text{Co}_1$  multilayer, whereas for increasing Co thicknesses, the average magnetic moments decrease. In addition to the concentration dependence, a correlation between the magnetic moments and the thickness of the Fe and Co layers can also be expected. A simple argument for this is that if the thickness of the layers were 1 ML each, it would correspond to an ordered  $\text{Fe}_{0.5}\text{Co}_{0.5}$  bulk alloy where the average magnetic moment can be found in Fig.6.1 to be  $\sim 2.4 \mu_B$  whereas for very thick layers the material can be seen as sepa-

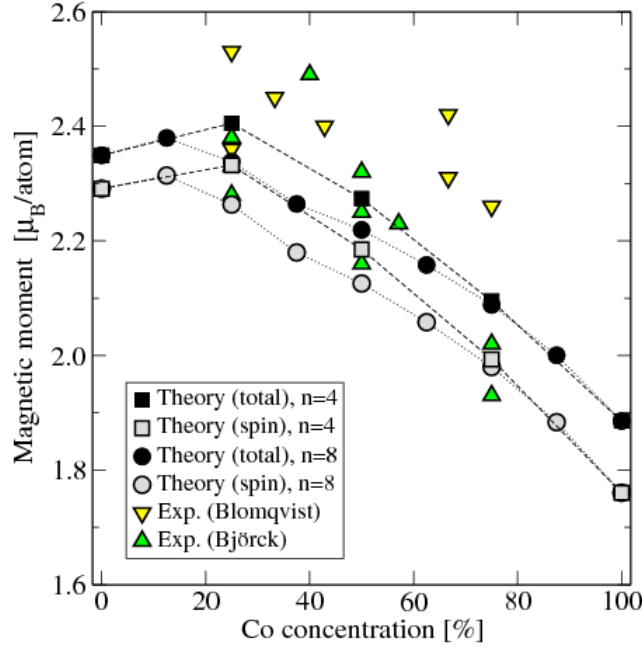


Figure 6.2: Calculated spin and total magnetic moments for bcc  $\text{Fe}_n/\text{Co}_m(001)$  superlattices, for  $n + m = 4$  and 8, as a function of the Co concentration.

rated chunks of Fe and Co and the average magnetic moment would then be  $\sim 2.0 \mu_B$ . This can be seen from the differences between 8 ML thick systems compared to the systems with a thickness of 4 ML in Fig. 6.2.

The increase of the magnetic moment for the thinner systems, which have a larger ratio of interfaces, indicates that the enhancement of the Fe spin moments are confined to a small region close to the interface. The behaviour of Fe spin moments close to Fe/Co interfaces will be discussed further in Sec. 6.5, in connection with the results for emedded Fe clusters.

### 6.4.2 Hyperfine fields

The hyperfine field is calculated from the difference between the spin-up and spin-down densities at the atom core. In many systems, the hyperfine field of Fe is proportional to the spin moment but that is not the case for Fe in Fe-Co alloys. In Fig. 6.3 experimental results for the hyperfine field of Fe as a function of Co concentration in Fe-Co alloys are shown. Although Fig. 6.3 looks quite similar to the behaviour of the average magnetic moments for Fe-Co alloys, it is important to keep in mind that the spin moment for Fe does not behave as the data in Fig. 6.3 at all. As mentioned in earlier sections, the spin moment of Fe increases monotonically from  $2.2\mu_B$  to a value of  $\sim 3\mu_B$  for a Co concentration of 50% where it saturates. In **Paper VI** we report on a combined theoretical and experimental study of the hyperfine fields for a selection

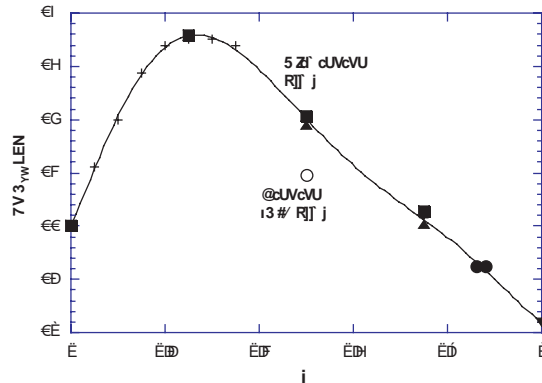


Figure 6.3: Measured hyperfine field distribution for Fe in bulk Fe-Co alloys.

of Fe-Co superlattices. The calculations suggest that the hyperfine field of the Fe atoms depend strongly on the short-range order. From the calculated hyperfine field profiles for two different multilayer configurations, as shown in Fig. 6.4, with varied layer thickness and degree of interface alloying, it seems like the hyperfine field is in fact determined by the local concentration of the nearest and next-nearest neighbours surrounding the Fe atoms. The sensitivity of the hyperfine field with respect to the short-range order makes the hyperfine field a very good probe for examining interface roughness which will be discussed below.

### 6.4.3 Interface roughness

Even though the chemical composition of a multilayer can be quite well regulated, full control over the growth process often proves very difficult to achieve. In practice, the interfaces of grown multilayers are almost always slightly rough due to structural distortions and chemical intermixing.

Structural distortions in multilayers are caused either by size mismatch between the different species or by competing structural preferences. Co, which is meta-stable in bcc grows nicely when deposited on top of a Fe layer, but as the thickness of the Co increases, the structure becomes increasingly distorted. As a result, it has been argued that Fe-Co multilayer interfaces are more distorted when growing Fe on top of Co than vice versa. Distortions from the perfect lattice can be calculated with electronic structure methods allowing for force relaxations. In **Paper V** the equilibrium geometry for a  $\text{Fe}_4\text{Co}_4$  multilayer was calculated with first principles calculations. It was found that in the case of Fe-Co multilayers, the small size mismatch between Fe and Co atoms cause only small distortions, with a maximum deviation of **2%** from

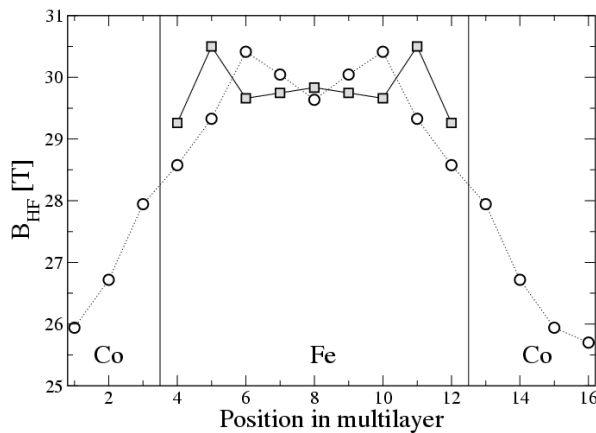


Figure 6.4: Calculated hyperfine fields for Fe atoms in an  $\text{Fe}_9\text{Co}_7$  multilayer. Squares correspond to values in a perfect multilayer while the circles correspond to hyperfine fields for an intermixed multilayer.

the perfect bcc lattice. The effect of the distortion on the magnetic properties was also calculated to be very small, affecting the average magnetic moments with less than 2% .

Due to the difficulties of determining the chemical intermixing experimentally, electronic structure calculations can prove a very valuable tool for this purpose. The perhaps most straight forward way of determining the interface characteristics theoretically is to use force relaxations, as mentioned above, or simulations based on calculated mixing energies. The roughness can however also be determined in a more indirect way by modelling the interface theoretically and calculate properties, such as magnetic moments, that can then be compared with experimental data. This latter approach can give a very good estimate of the interface roughness and intermixing and has successfully been used on i.e. Fe-V multilayer systems[53]. In order to succeed with this approach two criteria have to be met. First, the calculated property need to be sensitive to the interface properties, as an example the spin moment of Co would be a bad choice to probe the Fe-Co interface since the moment does not change much regardless of the chemical environment. The second criteria is that it must be possible to calculate the property with good agreement with the experiments, so that a comparison can be made. As was shown in the preceding section, the hyperfine field of Fe is very sensitive to the short-range order and thus also to the interface roughness in a Fe-Co multilayer. Unfortunately, the difference between the calculated and the measured hyperfine fields for Fe-Co systems makes it difficult to allow for a comparison based on the interface roughness.

In **Paper VI** we therefore compare the experimental results with an interface model where the modelled field is calculated not from first-principles calculations, but from experimental values for bulk Fe-Co alloys as displayed

in Fig. 6.3. In short, the model works as follows. By modelling the chemical composition across the Fe-Co interface, a concentration profile can be obtained. From the profile, the concentration profile can be calculated and the local concentration for Fe atoms in the intermixed layers can be obtained. The hyperfine field from the Fe atoms in each of the layers can then be obtained from the hyperfine field function in Fig. 6.3. The interface model used in **Paper VI** was constructed by considering the process of diffusion of atoms from one atomic layer to surrounding atomic layers. If the diffusion of atoms from one atomic layer is assumed to be isotropic and stochastic, the diffusion of each single atom can be viewed as a random walk process. Since the number of atoms in the atomic layer is very large,<sup>2</sup> the random walks of the atoms can be summed up into a normal distribution according to the Central Limit Theorem[54]. The distribution of atoms from the chosen atomic layer can be described by a Gaussian function with a chosen variance. Such a Gaussian function can then be assigned to each atomic layer in the multilayer geometry and the resulting concentration profile can readily be obtained by summing up all the normal distributions. Since all layers have been described with identical Gaussian curves, this model makes it possible to express the interface alloying with only one parameter which determines the variance of the Gaussians.

A set of concentration profiles, obtained from the model above, and the corresponding hyperfine field spectra for a  $\text{Fe}_5\text{Co}_9$  multilayer can be seen in Fig. 6.5. Here the parameter used is  $\Gamma_C$ , which corresponds to the full width at half maximum of the Gaussian function. The modelled hyperfine field spectra can be compared to the experimentally obtained spectra to find a corresponding  $\Gamma_C$ , which in this case was estimated to be  $\sim 1$  ML.

## 6.5 Embedded clusters

In a series of experiments, Binns and coworkers[55–57] have examined the magnetic properties of Fe clusters, deposited on an highly oriented pyrolytic graphite (HOPG) substrate, and embedded in Co. The clusters are created in a gas aggregation cluster source[58] and are then mass-filtered. The magnetic properties of the cluster based samples have then been examined using XMCD so that element specific information about the Fe atoms are achieved. They report an increase in the spin moments and an even larger relative enhancement of the orbital moments in comparison with bulk Fe. In **Paper VII** we have present results from calculations on similar systems. The Fe clusters were covered by Co in the experimental situation, and in our calculations we assume that the amount of Co is so large that the Fe clusters are isolated from other clusters, and fully embedded in Co. In the calculations, a perfect

---

<sup>2</sup>Usually these kinds of multilayers has an area of several millimeters which in the case of Fe would correspond to more than  $10^{13}$  atoms in each atomic layer

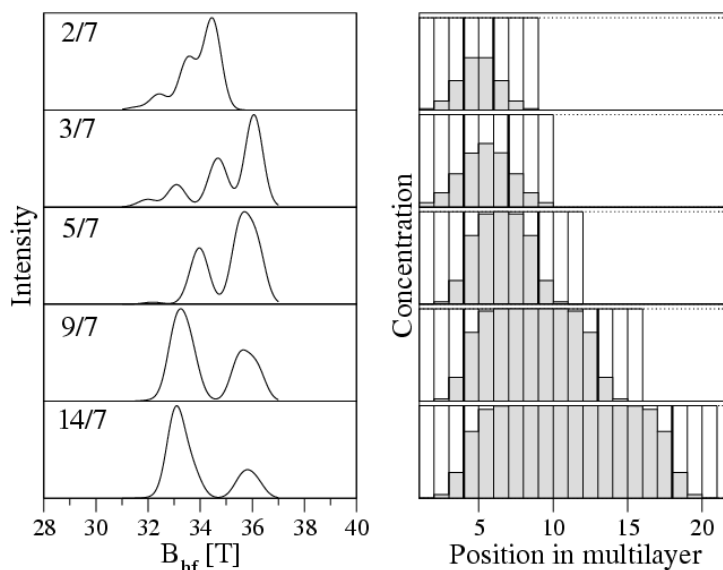


Figure 6.5: Simulated hyperfine field distribution for Fe, and corresponding layer concentration profile in interface alloyed Fe-Co multilayers. Gray bars correspond to the Fe concentration in each layer.

bcc structure was assumed, an assumption that has been supported by recent studies.[59]

Both experimental and calculated average magnetic moments are shown in Fig. 6.6. Given that the size and shape of the experimental clusters are not known exactly, the calculated average moments can be said to be in good agreement with the corresponding experimental values. Even for cluster sizes as large as 700 atoms there is a significant enhancement of the magnetic moments compared to the bulk Fe value.

How the spin moments of the Fe clusters are affected by the Fe-Co interface can be seen in Fig. 6.7 where the calculated magnetic profile for Fe clusters with sizes between 15 to 137 atoms, embedded in a Co host is displayed. In the same way as Fe spin moments are enhanced at a Fe-Co interface in a multilayer, Fe atoms in a cluster close to the Co interface exhibit spin moments well above the bulk value of pure Fe whereas the spin moments of the Co atoms stay virtually constant. The orbital moments for the Fe atoms in the same clusters are not enhanced at the interface.

A difference between the cluster interface and the multilayer interface is that since the considered multilayers all have the surface normal in the (001) direction, all interface Fe atoms in an Fe-Co multilayer have four Co atoms and four Fe atoms as nearest neighbours, whereas the composition of the nearest neighbours for Fe atom in a cluster interface can be different, depending on the position of the atom and the size of the cluster. By comparing the magnitude of the spin moment for Fe atoms situated at different sites in the clusters,

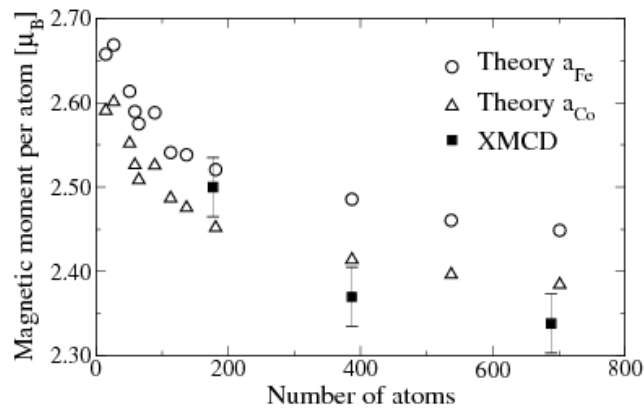


Figure 6.6: Calculated and measured average magnetic moments for Fe clusters embedded in a Co matrix.

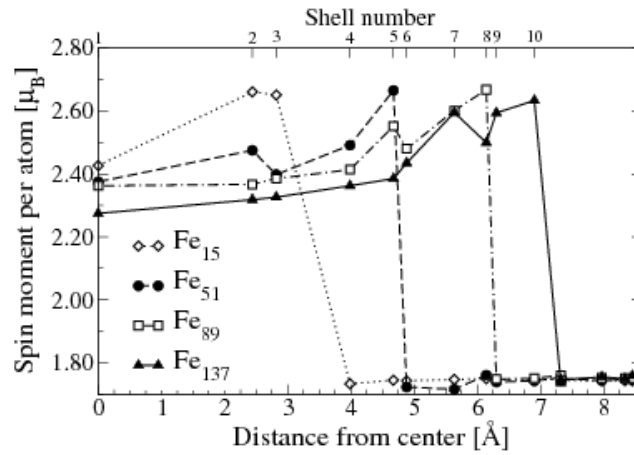


Figure 6.7: Local spin moment per atom for each shell for different sizes of Fe clusters embedded in Co. The calculated individual Fe moments increase up to  $\sim 2.65 \mu_B/\text{atom}$  for atoms close to the Fe-Co interface. The Co atoms have almost constant moments of about  $\sim 1.75 \mu_B/\text{atom}$ .

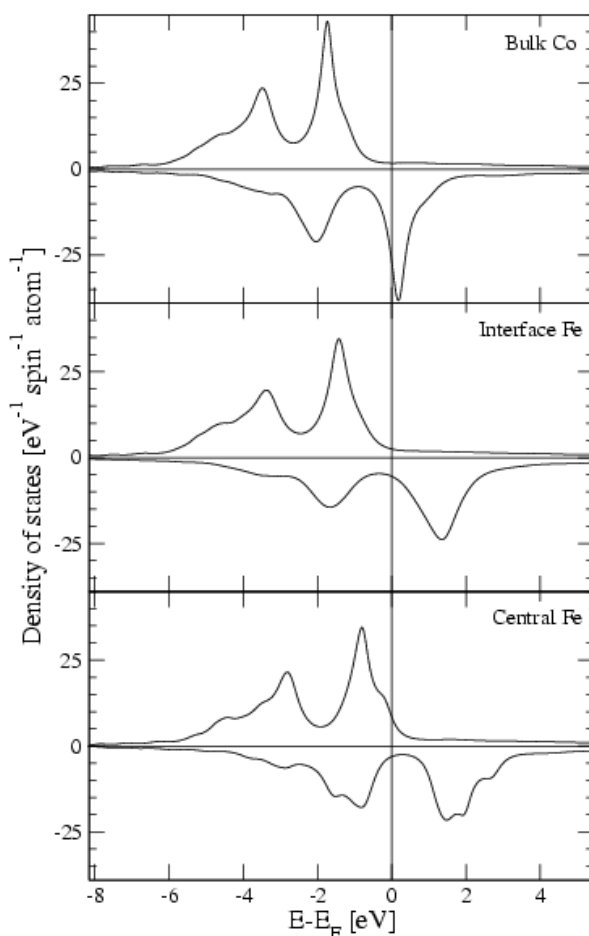


Figure 6.8: Local density of states for Fe atom in the center and at the interface of a 27 atom cluster and for a bulk bcc Co atom.

in relation to the nearest-neighbour composition it is found that the spin moment of the Fe atom is indeed very dependent on the number of Co atoms present in the nearest-neighbour shell. The composition of the next nearest neighbours also contributes to the spin moment but only to a very small part.

The cause of the enhancement of the Fe atoms at the cluster interface can be explained by examining the local density of states for the Fe atoms, which are shown in Fig. 6.8 for a central atom and an interface atom in a 27 atom Fe cluster. For comparison the LDOS for bulk bcc Co are also shown. Although the Fe atom at the interface with Co has similar features as the Fe atom at the center of the cluster, there is a marked difference in that the band filling is much higher. In particular one encounters a situation where the spin-up band of the interface Fe is full. The limited charge transfer between atoms atom in these systems (there is a small charge transfer of 0.05 electrons from the interface Fe atom to Co) implies that the interface Fe atom has transferred

some of its spin down electrons to spin up electrons, with an increased spin moment as a result. Co atoms at the interface have a DOS that is very similar to the DOS of bulk bcc Co.

The hybridization effects between Fe and Co can be explained in a simple model by the higher number of electrons of the Co atom which causes the valence bands to be more localized than the valence bands of Fe atoms. Fe atoms with Co neighbours will then have smaller wavefunction overlap compared to a case with only Fe atoms. The decreased overlap cause a narrowing of the bands which in the case of Fe fills the majority spin band at the cost of the minority spins.

### 6.5.1 Modelling the maximum moment

From the calculations of the Fe clusters embedded in Co it is apparent that the average magnetic moment per atom encompasses the bulk limit of  $2.45\mu_B$  for cluster sizes of up to  $\sim 100$  atoms. However the results above also points out two important factors that limits the magnetic moment for a Fe-Co cluster based material. The limiting factors are that the Co moments remain unchanged to a value of  $\sim 1.8\mu_B$  per atom and the fact that the enhancement of the Fe spin moments is caused by a close proximity to Co atoms. This causes a conflicting situation where on one hand many Co atoms are needed in order to increase the magnetic moments of the Fe cluster but on the other hand, the number of Co atoms should be minimized in order to achieve a high average magnetic moment in the material.

From a simple assumption of close packed spherical clusters, we modelled the average moment of a system consisting of cluster and surrounding matrix atoms by including a number of Co atoms, corresponding to 25% of the cluster atoms when the average magnetic moment was calculated. With this model, the average magnetic moment for a cluster based alloy is calculated to be larger than  $2.45\mu_B$  for cluster sizes up to  $\sim 50$  atoms. The simple model used above does however not take into account the possible effect of interactions between neighbouring clusters. In reality, it might be difficult to retain the high moments achieved within our simplified model, since for the low Co concentration that was considered in the model, it is not certain that the Fe clusters will have the same coordination of Co neighbours as in the model case. Instead, the clusters may have more Fe neighbours, which can result in a decrease of the moments. As a test of the effect of cluster-cluster interactions, a supercell calculation for a 15 atom Fe cluster surrounded by 25% Co was performed and the average magnetic moment for this system is only  $2.40\mu_B$  per atom which is lower than the estimation from our simplified model which predicted  $2.65\mu_B$ . Since the average moment for this close packed structure of the 15 atom Fe clusters decreased significantly from the non-interacting cluster model, it can be expected that the average moment would decrease for other cluster sizes as well. This indicates that it is unlikely to obtain saturation

magnetizations exceeding the current limit of  $\sim 2.45$  T for realistic systems of bcc Fe clusters embedded in bcc Co.

### 6.5.2 Alloying the embedding matrix

The results in the previous section indicate that the largest impediment for achieving large magnetic moments for a cluster based compound is not the clusters itself but instead the low moment of the surrounding matrix. Alloying the Co matrix with Fe would increase the magnetic moment, but then the question arises whether an Fe-Co alloy as a matrix would still cause an enhancement of the spin moments of the Fe atoms in the clusters. The influence of the magnetic moments of embedded Fe clusters when the embedding Co matrix is alloyed with Fe has been studied in detail in **Paper VIII**

The magnetic profile for Fe clusters containing 51 atoms embedded in an Fe-Co alloy, as is displayed in Fig. 6.9, shows that the magnetic moment of Fe atoms situated at the interface is not as large as when the embedding matrix consists of pure Co. However, there is still an enhancement of the spin moment compared to bulk Fe. A decrease of the magnetic moment for the interfacial layers of the alloyed matrix can also be seen. These behaviours can be explained by the importance of the short range order for Fe atoms mentioned earlier. Comparing with the case of a pure Co matrix, the effective number of Co neighbours for an interface Fe atom decreases with an increased concentration of Fe in the matrix. As an example, an interface Fe atom that may have four Co neighbours in the case of a pure Co host, will instead have a local environment corresponding to two Co neighbours if the matrix is alloyed with 50% Fe. The decrease of the moment of the alloyed matrix close to the interface comes from the opposite effect; an increase of the number of Fe neighbours for matrix atoms close to the interface.

The conclusion from Fig. 6.9 is that despite substituting the Co matrix to an Fe-Co alloy, the spin moments of the interface Fe atoms on the cluster are still enhanced. The total effect of the spin moment enhancement on the average magnetic moments for the embedded clusters can be seen in Fig. 6.10(a). Since the enhancement of the cluster spin moment is largest for the pure Co matrix, the highest average cluster moments are found for the Fe clusters embedded in pure Co. There is however a significant enhancement, compared to bulk Fe, even for the alloyed matrix. This shows that despite the relatively high concentration of Fe in the host matrix, the embedded Fe clusters have quite large average magnetic moments.

When the embedding matrix is included in the average magnetic moment, using the close packed model described in the previous section, as shown in Fig. 6.10(b), the highest average moment is actually found for the 50% Fe matrix. Even though the composition in Fig. 6.10(b) is calculated assuming that 25% of the material consist of matrix atoms, an advantage with a large moment matrix is that the amount of matrix material can be increased with-

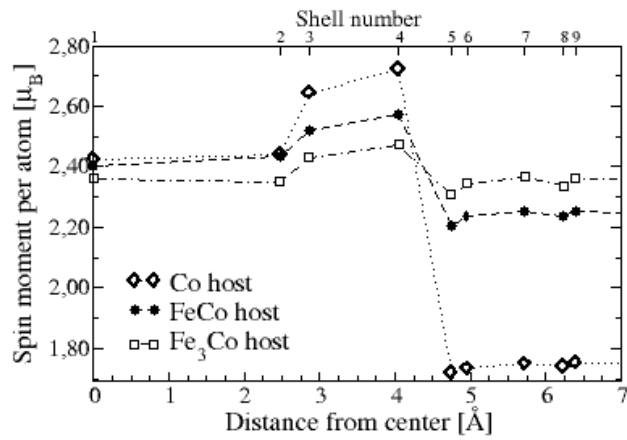
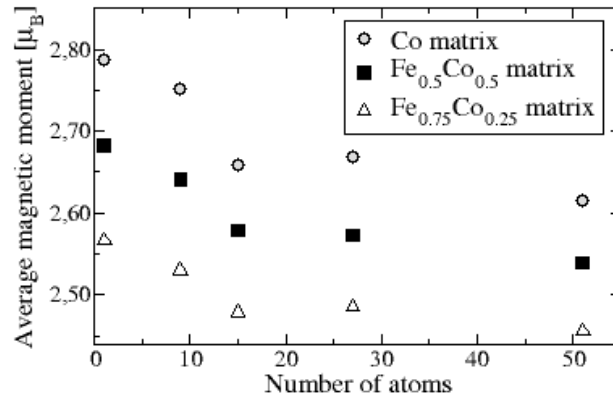
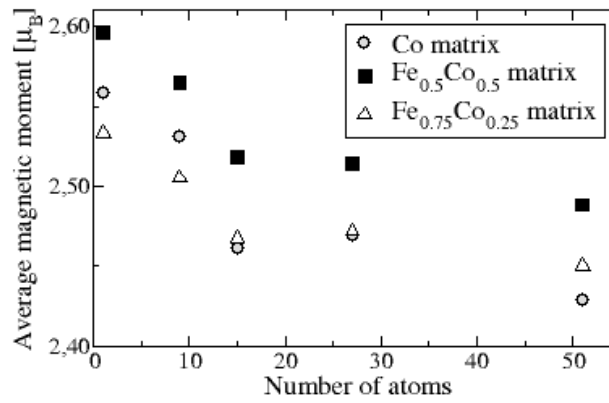


Figure 6.9: Magnetic profile of a 51 atom Fe cluster embedded in a Co matrix (diamonds), a Fe<sub>50</sub>Co<sub>50</sub> alloy (circles) and a Fe<sub>75</sub>Co<sub>25</sub> alloy (squares).

out lowering the average magnetic moment too much. Increasing the volume of matrix material also separates the clusters more, which leads to less risk for cluster-cluster interactions that reduce the cluster moments. These studies, discussed in full detail in **Paper VIII**, indicates that it is in fact not unlikely to tune the magnetic moments of materials based on embedded Fe clusters in a Fe-Co matrix to obtain saturation moments larger than what is given by the Slater-Pauling curve.



(a)



(b)

Figure 6.10: Average magnetic moments for only clusters (a) and clusters and 25% matrix material (b).



## 7. Non-collinear magnetism

Even though there is no principal restriction for a magnetic material to align its spins along a global spin axis, the majority of magnetic materials do in fact exhibit a collinear magnetic ordering. In this, and the following chapter, we will discuss mechanisms that cause a material to stabilize in a non-collinear magnetic ordering.

### 7.1 Criteria for non-collinear magnetism

As was discussed in connection to the derivation of the Stoner theory, a system can gain in energy by decreasing the density of states at the Fermi energy, which can result in the stabilization of a ferromagnetic state. Furthermore, it was also shown that strong nesting features of the Fermi surface of a material can stabilize anti-ferromagnetic structures or spin-density waves. In this section, we will discuss if these mechanisms also can cause a stabilization of a non-collinear magnetic state. As a result, we will identify two criteria for stabilizing a non-collinear magnetic structure, where the driving mechanism is hybridization between bands close to the Fermi energy. A more detailed discussion on these criteria is presented in **Paper IX**.

The non-collinear magnetic structures considered in this discussion are spin spirals. A spin spiral is defined as a magnetization density, expressed in cartesian coordinates,

$$\mathbf{m}(\mathbf{r}) = m(\mathbf{r})[\cos(\mathbf{q} \cdot \mathbf{R} + \phi)\sin\theta, \cos(\mathbf{q} \cdot \mathbf{R} + \phi)\sin\theta, \cos\theta], \quad (7.1)$$

where  $m$  is the magnitude of the magnetic moment,  $\phi$  and  $\theta$  are polar angles,  $\mathbf{R}$  is a lattice vector and  $\mathbf{q}$  is the wave vector characterizing the spin spiral. The usefulness of the spin spiral comes from the fact that a translational operation  $\mathcal{T}$  with a lattice vector  $\mathbf{R}$  on a spin spiral corresponds to a spin rotation,  $\mathcal{R}_\phi$  where  $\phi = \mathbf{q} \cdot \mathbf{R}$ . Using the symmetry properties of the spin spiral, it can be shown[60, 61] that it is possible to construct Bloch spinors that diagonalize the Hamiltonian as

$$\psi_{\mathbf{k}}(\mathbf{r}) = e^{i\mathbf{k} \cdot \mathbf{r}} \begin{pmatrix} e^{-i\mathbf{q} \cdot \mathbf{r}/2} \alpha_{\mathbf{k}}(\mathbf{r}) \\ e^{i\mathbf{q} \cdot \mathbf{r}/2} \beta_{\mathbf{k}}(\mathbf{r}) \end{pmatrix} \quad (7.2)$$

where  $\alpha_{\mathbf{k}}(\mathbf{r})$  and  $\beta_{\mathbf{k}}(\mathbf{r})$  are the periodic functions for the spin-up and spin-down components of the spinor. In the case of  $\mathbf{q} = 0$ , the spiral corresponds to a ferromagnetic solution.

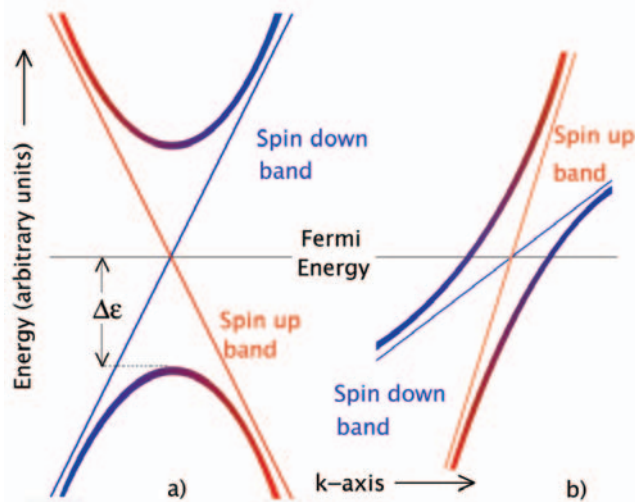


*Figure 7.1:* Schematic energy band crossings for a hypothetical material. The straight thin lines correspond to two orthogonal spin-up and spin-down bands in a ferromagnetic state. When a non-collinear component of the magnetization is present, the two spin channels may hybridize which can result in the opening of a gap at the Fermi level and a lowering of the band energy. The corresponding hybridized bands are shown in the figure as the thick bands.

In Fig. 7.1, two different scenarios for a band crossing at the Fermi energy for a hypothetical, ferromagnetic element are displayed. The crossing bands have different characters, where one of the bands is a spin-up band while the other is a spin-down band. Since, in a collinear state, the spin-up and spin-down components are orthogonal<sup>1</sup>, they can not hybridize with each other. In a non-collinear state, such as one described by spin spirals, the wavefunctions are expressed by spinors which do not possess pure spin-up or spin-down character, and the two spin components are thus allowed to hybridize. Hybridized spin spiral bands can be seen as the parabolic curves in Fig. 7.1. Compared to the ferromagnetic bands, the hybridized bands open up a gap, and the repulsion between the hybridized bands pushes them apart. If the crossing occurs close to the Fermi level, the hybridization results in a gap where the upper band is pushed above the Fermi energy and will thus not contribute to the total energy, whereas the lower band will be pushed down from the Fermi energy, which will lower the total energy.

From this discussion we can deduce two criteria that need to be fulfilled for the stabilization of a non-collinear magnetic structure. In order for this hybridization to take place, both spin-up and spin-down bands must cross the Fermi level. This condition excludes strong ferromagnets such as hcp Co and fcc Ni. Further, the kinetic energy gained by the gap opening mechanism is to

<sup>1</sup>As was discussed in 2.4

a certain extent balanced by a cost in the exchange energy due to that hybridized bands lead to reduced moments. In order for the energy gain to be sufficiently large, there need to be prominent nesting features between the spin-up and spin-down bands, since if the spin-up and spin-down bands can coincide for a rigid shift in  $k$ -space, many  $\mathbf{k}$ -points can be involved in the energy lowering process.

The effectiveness of the described mechanism have been verified by electronic structure calculations, reported in **Paper IX**, for a variety of transition metals where the two criteria mentioned above have been fulfilled by tuning the exchange splitting of the examined materials by either changing the volume, or by using fixed spin calculations.

## 7.2 TiCo<sub>2</sub>Se<sub>2</sub>

The criteria described above are not only applicable to metals under very special conditions, but can exist in certain compounds under normal circumstances as well. Such an example is TiCo<sub>2</sub>Se<sub>2</sub> whose magnetic properties are examined in **Paper X**. Due to the crystal structure of TiCo<sub>2</sub>Se<sub>2</sub>, a layered tetragonal I4/mmm structure, the compound exhibits quasi two-dimensional behaviour. The magnetism is driven by the Co atoms which sit in a square lattice in two dimensions. In the plane, the Co atoms couple ferromagnetically to each other[62], but the large distances between the Co planes,  $\sim 7\text{\AA}$ , an interesting ordering is found along the out-of-plane axis. According to experiments, the magnetization axis turns with  $\sim 121^\circ$  between the Co planes. This corresponds to a spin spiral structure with  $\mathbf{q} = (0, 0, 0.7)2\pi/c$ . It is very unusual for Co compounds to exhibit non-collinear magnetic ordering, as a matter of fact this is the only known example.

These experimental findings were accompanied by non-collinear APW+lo calculations, where it was found that the ground state was not a spin spiral, but a collinear anti-ferromagnet. The calculated energy difference between the antiferromagnetic structure and the experimentally found structure is small,  $\sim 0.1$  mRy, and a study of the Fermi surface indicate that the spin spiral may be stabilized by the effect discussed in Section 7.1.

## 7.3 TbNi<sub>5</sub>

The magnetic structure of the rare-earth compound TbNi<sub>5</sub>, that has been studied in **Paper XI**, can be explained in terms of nesting between spin-up and spin-down Fermi surfaces. Neutron diffraction measurements indicate that the magnetic structure is a helical spin spiral with an incommensurate wavevector  $\mathbf{q} = (0, 0, 0.02)$ , and with a total magnetic moment of  $8.4\mu_B$ .

The experimental findings have been accompanied by electronic structure calculations, using APW+lo and LMTO-ASA methods. The magnetic moment comes mainly from the localized  $4f$ -electrons of the Tb, with only a small induced moment on the Ni atoms coupled antiferromagnetic to the Tb moment. The calculated magnetic ground state, from APW+lo, is a spin spiral with a wavevector  $\mathbf{q} = (0, 0, 0.06)$ , albeit with a small energy difference of 0.11 mRy compared to a ferromagnetic solution. From a Fermi surface analysis based on the LMTO-ASA band structure for the ferromagnetic solution, a nesting vector  $\mathbf{q} = (0, 0, 0.03)$  between the spin-up and the spin-down sheets were found. Since this latter  $\mathbf{q}$  is very close to the experimentally observed wavevector, it is sensible to believe that the noncollinear behaviour is indeed an effect of strong Fermi surface nesting.

## 7.4 Fcc Fe

The perhaps most known material that exhibits non-collinear magnetism is fcc Fe. At ambient conditions Fe has a bcc structure, so an Fe based fcc structure can either be found for elevated temperatures where the fcc phase is stable between  $900^\circ$ - $1400^\circ$ , or in alloys. A well known example of an fcc Fe alloy is stainless steel which is obtained by adding  $\sim 10$ - $15\%$  Cr and  $5 - 10\%$  Ni. Alloying Fe with  $\sim 35\%$  Ni results in another fcc-based material with technological relevance, Invar, which has very low thermal expansion compared to other metals. The anomalous behaviour of Invar alloys have been shown to originate from a non-collinear magnetic ordering[63].

Pure fcc Fe has been stabilized as precipitates inside a fcc Cu matrix[64], where the spherically shaped Fe particles have a mean diameter of 50 nm. The magnetic ground state for these precipitates have been determined to be a spin spiral with a wave vector

$$\mathbf{q}_{exp} = (0.10, 0, 1) \frac{2\pi}{a}, \quad (7.3)$$

where  $a$  is the lattice constant of the surrounding fcc Cu matrix, which is assumed to be inherited by the Fe precipitates. The ground state is thus close to a collinear antiferromagnet, which would correspond to a wave vector of  $\mathbf{q}_{AF} = (0, 0, 1)2\pi/a$ .

Theoretically, the fcc Fe system has been studied by a large number of methods with a wide spread between the obtained results. In earlier calculations, the experimental situation with precipitated Fe particles, have only been accounted for by simply using the lattice parameter of Cu while performing supercell or spin-spiral calculations assuming an infinite particle size. In **Paper XII** we report on non-collinear calculations of fcc Fe, using the RS-LMTO-ASA method, where we have tried to mimic the experimental situation to a larger extent than what has been done before, by considering a small

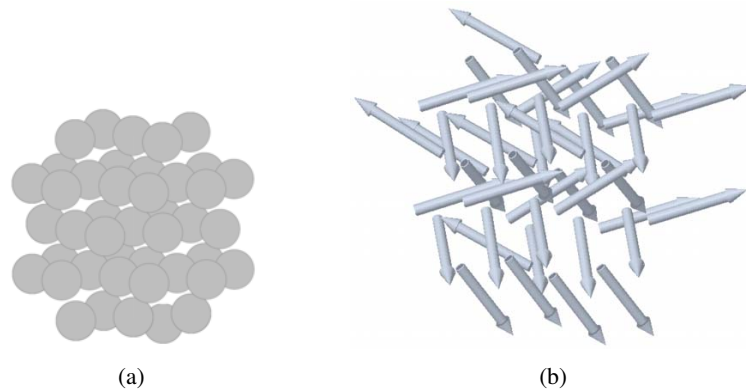


Figure 7.2: The geometry of the embedded Fe cluster (a) , and the magnetic moments for the calculated ground state (b).

Fe cluster embedded in an fcc Cu matrix. In the reported study we considered clusters of 43 Fe atoms sitting on the underlying fcc lattice of the Cu matrix, where the cluster shape is as spherical as possible corresponding to a central atom surrounded by three shells of nearest neighbours. The geometry of the studied cluster is shown in Fig. 7.2(b).

A comparison between different collinear configurations of the cluster shows that an antiferromagnetic solution is preferred, and that many different configurations lie very close in energy. The most stable collinear solution, of those considered, was found to be a configuration where the moments of the atoms being nearest-neighbours to the central atom couple parallel to each other but antiferromagnetically to the remaining atoms. The energy difference compared to other antiferromagnetic solutions is in the order of a few mRy/atom and less.

Non-collinear calculations have also been performed for the cluster. Several starting configurations were used in order to avoid local minima, and the moments of the cluster atoms were allowed to rotate freely. The resulting magnetic structure, with the lowest energy is shown in Fig. 7.2(a). A majority of the considered starting guesses ended up with a similar magnetic orders as the one displayed in Fig. 7.2(a) which makes it a reasonable assumption that this configuration is close to a global minimum.

The magnetic structure in Fig. 7.2(a) looks a bit chaotic at first glance and it is not obvious how to analyze the magnetic ordering in the cluster. For this system without periodicity, the obtained magnetic structure can be characterized by the angles  $\theta_{ij}$  between two different magnetic moments,  $m_i$  and  $m_j$

$$\theta_{ij} = \arccos(\hat{m}_i \cdot \hat{m}_j). \quad (7.4)$$

The calculated structure can be visualized as a histogram over all  $\theta_{ij}$  for the system, as is done in Fig. 7.3. In this figure we see a concentration of an-

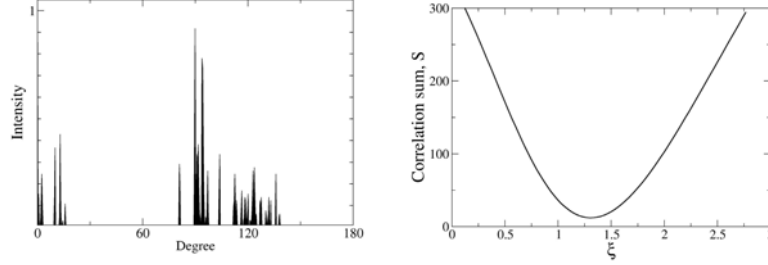


Figure 7.3: Histogram over  $\theta_{ij}$  for the calculated magnetic ground state, and correlation sum  $S(\xi)$ .

gles between  $\sim 0^\circ$  and  $\sim 15^\circ$ , around  $\sim 90^\circ$ , and spread out between  $\sim 110^\circ$  to  $\sim 140^\circ$ . This  $\theta_{ij}$  distribution can be compared to other magnetic orderings, by introducing a spin correlation sum  $S$  as

$$S(\{m\}, \{m^0\}) = \frac{1}{n(n-1)} \sum_{i=1, n} \sum_{j \neq i} (\hat{m}_i \cdot \hat{m}_j - \hat{m}_i^0 \cdot \hat{m}_j^0)^2, \quad (7.5)$$

where  $n$  is the number of atoms and  $\{m\}$  and  $\{m^0\}$  are two sets of magnetic moments for these  $n$  atoms. The sum in Eqn. 7.5 is then a measure of how similar the two sets  $\{m\}$  and  $\{m^0\}$  are, where  $S = 0$  would indicate that the sets are identical (or only differing by a global rotation). With the expression in Eqn. 7.5 we can empirically compare different proposed magnetic configurations  $\{m^0\}$  with our self-consistently calculated ground state structure  $\{m\}$ .

As reference magnetic structures  $\{m^0\}$ , we used several variations of antiferromagnetic orderings, helical spin density waves and multi- $\mathbf{q}$  orderings. The lowest  $S$  value was obtained for a  $3\mathbf{q}$  structure with a magnetic wave vector at the  $X$ -point. In general this type of  $3\mathbf{q}$  magnetic order is a superposition of the three oscillations

$$\mathbf{m}_{3\mathbf{q}}(\mathbf{r}) = \sum_i^3 \mathbf{m}_i e^{i\mathbf{q}_i \cdot \mathbf{r}}, \quad (7.6)$$

with wave vectors  $\mathbf{q}_1 = (100)2\pi/a$ ,  $\mathbf{q}_2 = (010)2\pi/a$ , and  $\mathbf{q}_3 = (001)2\pi/a$ . For the best reference structures, the three different moment amplitudes can be written as

$$\mathbf{m}_1 = m_0 \begin{pmatrix} 1 & 0 & \xi \end{pmatrix} \quad (7.7)$$

$$\mathbf{m}_2 = m_0 \begin{pmatrix} -1/2 & \sqrt{3}/2 & \xi \end{pmatrix} \quad (7.8)$$

$$\mathbf{m}_3 = m_0 \begin{pmatrix} -1/2 & -\sqrt{3}/2 & \xi \end{pmatrix}, \quad (7.9)$$

where  $\xi$  is a yet undefined parameter. When ignoring this third component, these three moment amplitudes form  $120^\circ$  angles with each other. This mag-

netic structure have a simple cubic unit cell with four inequivalent sites. In the case of  $\xi = 0$  three of the magnetic moments are of equal magnitude, lies in the  $xy$ -plane, and form  $120^\circ$  angles with each other, while the fourth has a vanishing magnitude. By evaluating  $S$  as a function of  $\xi$ , as displayed in Fig. 7.3, we find a low lying minimum at  $\xi=1.33$ , which then have a close correspondence with our calculated structure. In this structure the four sites have moments that form either an angle of  $124^\circ$  or  $92^\circ$ , with each other, which are shown together with the calculated angles in Fig. 7.3. When ignoring surface enhancements effects, the magnitudes are described well with this  $3\mathbf{q}$  model, with the magnetic moment on the site with almost perpendicular moment larger than the other three, which in turn are very similar.

For bulk fcc Fe with the lattice parameter of Cu, the obtained  $3\mathbf{q}$  structure found to be 0.2 mRy/atom higher in energy compared to the conventional  $3\mathbf{q}$  structure with  $109^\circ$  between the moments. This implies that the magnetic structure obtained from the cluster calculation is unique for small clusters.

Returning to the different configurations calculated self-consistently, it can be noted that the energy differences between the obtained configurations are very small, and can be considered degenerate within the energy resolution of the RS-LMTO-ASA method. As an example, a calculated solution, with a structure that fitted to the model above would yield angles of  $98^\circ$  and  $120^\circ$ , lies only 0.01mRy above the structure shown in Fig. 7.2(a).



## 8. Magnetic nanostructures

A common description of a nanostructure, is that the system has at least one dimension in the nanometer regime, and that it is manufactured or manipulated artificially. With this definition, a free molecule itself is not a nanostructure while a system where the same molecule is attached to leads on a surface is. Connecting to the materials studied so far in this thesis, multilayers and embedded clusters can be defined as nanostructures, or at least nanostructured materials.

The physics of nanostructures is mostly governed by effects due to reduced dimensionality, broken symmetries, and a large number of interfaces, and their behaviour is therefore not bulk-like. The constrained geometry present in nanostructures can also cause quantum mechanical effects such as quantum-well induced magnetism and quantum mirages.

In this chapter, the magnetic properties of nanostructures consisting of small metallic clusters supported on a surface will be discussed. With techniques such as scanning tunneling microscopy (STM)[65], atoms on surfaces can be manipulated and assembled to small clusters. With spin-polarized STM[66], a contrast depending on the alignment of the spins in the nanostructures can be obtained, which can be used to determine the magnetic ordering of the structure.

### 8.1 Reduced dimensionality

As an example of the lowered symmetry for a nanosystem, we can consider the surface depicted in Fig. 8.1. Atom A is placed in what can be called a bulk like environment with six nearest neighbours. Situated on the surface is atom B which has 4 nearest neighbours while the ad-atom C has only two nearest neighbours. This decreased coordination can change the physical properties of the atom drastically.

The effect of the decreased coordination number on the local density of states, can be estimated with a simple model calculation. The bandwidth of the local density of states is proportional to the square root of the second

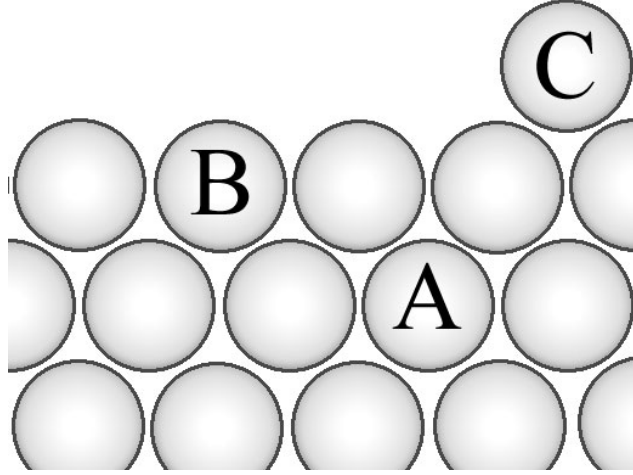


Figure 8.1: Schematic view of the coordination number for ad-atoms (C) and surface atoms (B) compared to more bulk like atoms (A).

moment of the LDOS<sup>1</sup> which is calculated as

$$m_i^2 = \sum_j \langle j|H|i\rangle \langle i|H|j\rangle. \quad (8.1)$$

Suppose that the Hamiltonian,  $H$  is in a tight-binding form with the only non-zero elements being a hopping term  $\beta$  for nearest-neighbours. If the coordination number for the atom is  $N$ , then by counting the possible hopping paths for the atom the second moment can readily be calculated as  $m_i^2 = N\beta^2$ . The reduced coordination number for atoms in surface nanostructures will thus cause a narrowing of the density of states compared to bulk atoms.

We showed earlier (in Chapter 5) that the magnetic ordering is sensitive to the shape of the density of states. In Fig. 8.2, schematic densities of states for d-like electrons, which can be used for illustrating the different scenarios that can happen with the electronic structure for an ad-atom, are shown. For simplicity, we will assume charge neutrality for the ad-atom in the following discussion.

First, we can consider the LDOS for an atom that in its bulk state is a weak ferromagnet. This is shown in the (A) panel of Fig. 8.2. A band narrowing for this atom causes a downward shift in energy for the majority band while the minority band is shifted up in energy. The result of the band narrowing in this situation is a transfer of spins from the minority to the majority band and an enhanced magnetic moment, which can be seen in panel (B). If the band narrowing is sufficiently large compared to the exchange splitting, the majority band will be completely filled, causing a transition to a strong ferromagnet. A

<sup>1</sup>See c.f. Ref.[28] for a thorough explanation on the moment expansion of the local density of states

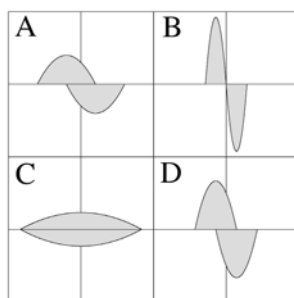


*Figure 8.2:* Examples of magnetic phase transitions due to band narrowing. (A) is a bulk weak ferromagnetic atom which becomes (B) at the surface. (C) is a non-magnetic bulk atom which becomes magnetic (D) at the surface due to band narrowing.

more spectacular effect can occur for atoms that in the bulk configuration are nonmagnetic. The lower figures of Fig. 8.2, displays the effect of the band narrowing for such a nonmagnetic atom in panel (C). Since the total number of electrons is constant, the narrowing of the band leads to an increase of the density of states at the Fermi level. If the resulting density of states at the Fermi level is large enough, the Stoner criterion (Eqn. 5.4) is fulfilled and the bands will be exchange split, causing a magnetic behaviour of the ad-atom which is seen in panel (D). If the DOS in the bulk configuration is very delocalized or if the band narrowing is too small, the atom stays non-magnetic.

## 8.2 Frustration

In Chapter 7 band hybridization effects as a possible cause for non-collinear magnetic ordering were discussed. Nanostructures lack translational symmetry and the band picture is therefore not completely valid. Due to the confined geometry of supported clusters, there is instead another important feature that can cause non-collinear magnetic ordering for these nanostructures, the presence of geometrical frustration.

The concept of frustration can be visualised by considering a network of three spins situated on an isolated, equilateral triangle, as depicted in Fig. 8.3. For this system of localized spins we can calculate the magnetic energy in terms of a Heisenberg Hamiltonian. If the exchange interaction,  $J$ , is the same for all spins the Hamiltonian is written as

$$H = - \sum_{i \neq j} J_{ij} \mathbf{s}_i \cdot \mathbf{s}_j = -J \mathbf{s}_1 \cdot \mathbf{s}_2 - J \mathbf{s}_2 \cdot \mathbf{s}_3 - J \mathbf{s}_3 \cdot \mathbf{s}_1 \quad (8.2)$$

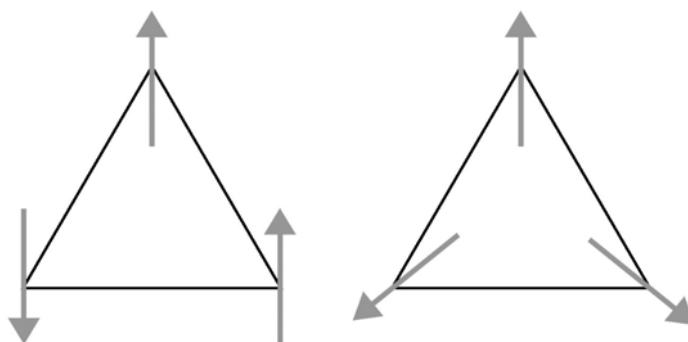


*Figure 8.3:* The left triangle displays a frustrated system, which result in the non-collinear state of the right panel, where the moments makes an angle of  $120^\circ$  with their neighbours.

where  $\mathbf{s}_i$  is the unit vector along the direction of the spin at site  $i$ . For a positive  $J$ , a ferromagnetic solution will have the lowest energy of  $-3J$ . If  $J$  is negative, then each spin want to couple antiferromagnetically with neighbouring spins, but as a result of the triangular geometry, it is impossible for all three spins to align antiparallel with both their neighbouring spins. A collinear arrangement with two of the spins pointing antiparallel to the third spin would result in an energy of  $-J$  which is larger than what the energy would be if all spins could simultaneously align antiferromagnetically to each other. The geometry can thus be said to frustrate the system by prohibiting it from obtaining the true ground state.

If the spins in Fig. 8.3 are not restricted to a collinear configuration, the lowest energy possible, is obtained by arranging the spins so that they makes an angle of  $120^\circ$  with each neighbour. The energy is then  $-\frac{3}{2}J$  and hence is lower than the collinear solution. For this particular system, we can see that a non-collinear ordered state is stabilized as an effect of the geometrical frustration.

The concept of geometrical frustration is far from restricted to this simple example and is important not only for the magnetic ordering but for structural and thermodynamic properties as well, especially for disordered materials.[67]

### 8.3 Substrates

The choice of substrate can be of large importance for the magnetic properties of supported clusters. In experimental situations, deposited clusters often conform to the structure of the underlying surface, so by varying the choice of substrate, the geometry of the cluster can be changed. Depending on the electronic structure of the surface, the energy bands of the surface can hybridize more or

less with the electrons of the deposited atoms. Most of the results presented in this chapter consider clusters supported on a noble-metal surface, Cu(111) or Au(111), where the hybridization between surface and cluster atoms are small. The limited hybridization allows for studies of the more intrinsic magnetic properties of the supported clusters. On the other hand, a substrate that hybridizes more with the deposited clusters can cause a major change of the magnetic properties of the clusters, as will be discussed in Sec. 8.6. The (111) surface direction is a close-packed direction in the fcc structure, and deposited atoms can thus be placed in positions corresponding to an equilateral triangular lattice, which according to Sec. 8.2 can cause geometrical frustration if the cluster atoms couple antiferromagnetically.

## 8.4 Cr, Mn, and Fe on Cu(111)

The scenario of geometrical frustration can be examined by depositing atoms that couple anti-ferromagnetically situated on a triangular lattice. As was mentioned in the previous section, an fcc(111) surface is a good template for a triangular lattice. Antiferromagnetic ordering can be expected for the elements in the middle of the  $3d$ -series. Cr, that has an antiferromagnetic spin-density wave ground state in bulk, and Mn that has a complex non-collinear ordering in a 58 atom unit cell as the bulk ground state are thus good candidates. Since Fe is known to order non-collinearly in the fcc structure while being ferromagnetic in bulk bcc, Fe might couple antiferromagnetically as well.

A monolayer can be seen as an intermediate between bulk and cluster, and previous calculations[68, 69] have predicted a monolayer of Cr on Cu(111) to order in a non-collinear structure with  $120^\circ$  between neighbouring moments, while a Mn monolayer orders row wise antiferromagnetically. A single monolayer of Fe on Cu(111) orders in a high-spin ferromagnetic configuration, with a transition to a low spin configuration when the layer thickness is increased beyond 3 monolayers.

The magnetic ordering of clusters of these transition metals supported on a Cu(111) surface has been examined in **Paper XIII and XIV**, and will be briefly review below.

Due to the reduced dimensionality, the atomic moments in the clusters can be expected to be large. This is indeed the case, as can be seen in Fig. 8.4, where the individual moments for the atoms in the considered clusters are shown as a function of the number of nearest neighbours. Mn is found to have the largest spin moment, which can be expected, considering the electronic configuration of the free atom, where Mn has the largest number of unpaired electrons. It can also be noted that the moments in Fig. 8.4 show an almost linear dependence of the number of nearest-neighbour atoms, albeit with different slopes for the three elements.

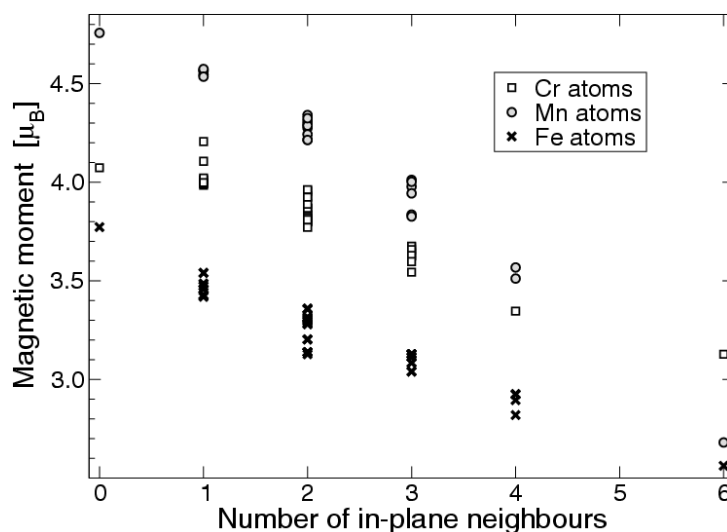


Figure 8.4: Spin moments, as a function of the number of nearest-neighbours, for atoms in Cr, Mn and Fe clusters supported on a Cu(111) surface.

The orbital moments have also been calculated for a selection of the clusters. The Fe clusters exhibit the largest orbital moments which also depend heavily on the coordination number, ranging from  $0.33\mu_B$  for a single ad-atom to  $0.06\mu_B$  for an Fe atom with six other Fe neighbours. The behaviour of enhanced spin and orbital moments is also noted for Fe clusters supported on a Ni(001) surface that has been studied in **Paper XVII**. The orbital moments for the Cr and Mn clusters were very small, of the order of  $0.01\mu_B$  per atom.

Regardless of the geometry, all Fe clusters were found to order ferromagnetically. The Cr and Mn clusters on the other hand, were found to exhibit an antiferromagnetic exchange coupling between nearest neighbours. An example of the antiferromagnetic coupling can be seen in Fig. 8.5(a), where a straight Mn trimer is shown. The geometry in Fig. 8.5(a), is similar to what was discussed in Sec. 8.2, and as a result the magnetic ground state of the triangle is indeed a non-collinear solution with an angle of  $120^\circ$  between the magnetic moments. The same magnetic structure was also obtained for Cr for the two geometries.

As the cluster sizes increase, the magnetic ordering of the Mn and Cr clusters become more complex. In the two examples mentioned above, the magnetic ordering can be described correctly with a nearest-neighbour Heisenberg Hamiltonian. The question is whether or not a Heisenberg Hamiltonian can explain the magnetic structure as the size of the clusters increase. This was tested by comparing our calculated magnetic configurations for certain cluster with the magnetic structure obtained from minimizing a Heisenberg Hamiltonian for different choices of nearest-neighbour exchange interactions. It was found that the ground state of several Cr clusters, such as those displayed in Fig. 8.6,

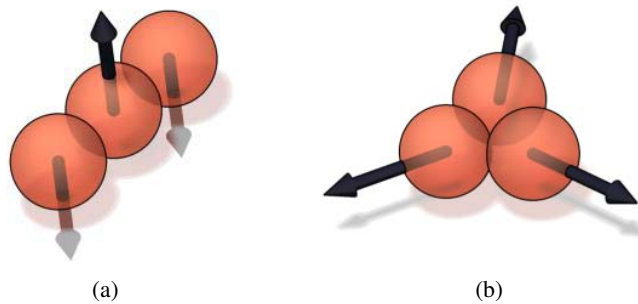


Figure 8.5: The magnetic ordering for three atom Mn clusters on a Cu(111) surface. Geometrical frustration causes non-collinear magnetic ordering for the triangle in (b).

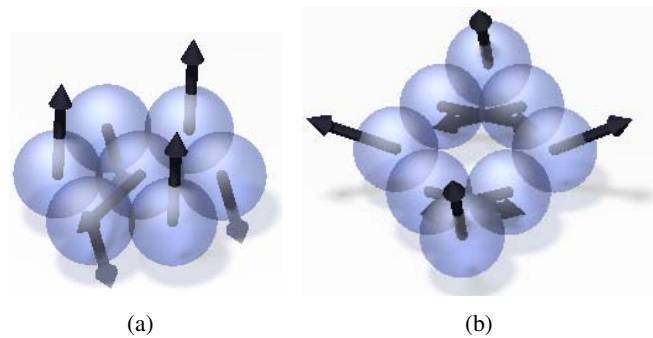


Figure 8.6: The calculated magnetic ground state for Cr clusters on a Cu(111) surface.

can be obtained from a Heisenberg Hamiltonian if the exchange parameters were scaled with respect to the local structure of the atoms. In addition to the non-collinear examples, there are also several cluster geometries where the atoms can order in a collinear antiferromagnetic configuration and can thus be predicted from a simple Heisenberg Hamiltonian. Although it is not shown here, the magnetic ordering in Mn clusters is however not always as easily described with a Heisenberg model.

The difference between the magnetic interactions of Cr and Mn can be illustrated with the tetrahedron shaped clusters shown in Fig. 8.7. The Fe pyramid (Fig. 8.7(a)) exhibits a ferromagnetic order. The atom situated on top of the pyramid has a magnetic moment of  $3.40\mu_B$  while the three Fe atoms closer to the Cu surface have a magnetic moment of  $3.11\mu_B$ . For the Mn cluster shown in Fig. 8.7(b), a non-collinear structure is found and for the Cr pyramid, shown in Fig. 8.7(c) a collinear antiferromagnetic solution is found.

A model Heisenberg Hamiltonian, as in Eqn. 5.8, with only antiferromagnetic nearest-neighbour exchange parameters,  $J_{ij}$ , yields a two-fold degenerate ground state, either a collinear antiferromagnet or a non-collinear tetragonal

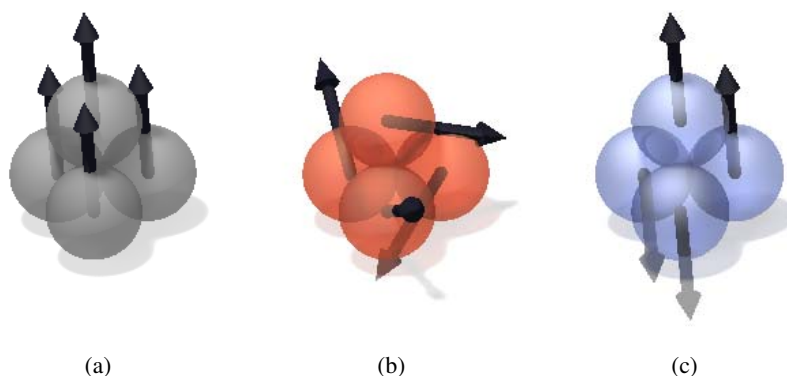


Figure 8.7: The calculated magnetic ordering for pyramid shaped clusters on a Cu(111) surface. Fig. 8.7(a) shows a Fe cluster with a ferromagnetic solution. Fig. 8.7(b) shows a Mn cluster and Fig. 8.7(c) shows the Cr pyramid.

configuration with  $109^\circ$  between neighbouring angles. The angles between the moments in the Mn pyramid are not exactly  $109^\circ$ , but instead around  $116^\circ$  between the base atoms close to the substrate and there are angles of about  $100^\circ$  between the base site and the top atom, which can be attributed to a larger moment for the top atom and thus a larger exchange interaction between top atom and a base atom compared to the  $J_{ij}$  between two base atoms. The difference in the total energy between the non-collinear ground state structure and the antiferromagnetic solution for the Mn cluster is 25 meV per atom while the corresponding difference for the Cr pyramid is 15 meV per atom in favor of the collinear antiferromagnetic structure. The fact that the antiferromagnetic and the non-collinear solutions are not degenerate indicates that the bilinear exchange terms  $J$  can not always describe the magnetic interactions between the atoms in supported magnetic clusters, a fact which previously has been suggested for magnetic dimers on surfaces.[70]

## 8.5 V on Cu(111)

V is in bulk non-magnetic, but theoretical studies have predicted V to become magnetic in free clusters and with exchange interactions changing between ferromagnetic and antiferromagnetic behaviour depending on the structure and size of the clusters. In **Paper XV** we present calculations on the magnetic ordering for V clusters supported on a Cu(111) surface. We find for straight clusters, such as a dimer or a trimer, that the V atoms are in fact magnetic and couple antiferromagnetically to their nearest-neighbours. The antiferromagnetic coupling causes a non-collinear magnetic structure, as was the case for Cr and Mn on Cu, for a frustrated equilateral triangular geometry.

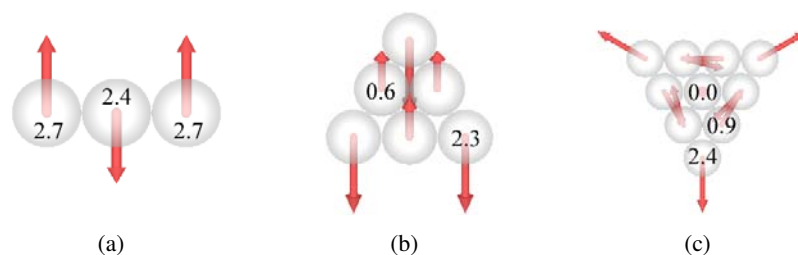


Figure 8.8: The magnetic order for V clusters on a Cu(111) surface. The numbers on the atoms indicate the calculated magnetic moment, (in  $\mu_B$ ).

As can be seen in Fig. 8.8, the behaviour of the V clusters differ from that of Cr and Mn as the cluster size increases. The magnetic moments of the different atoms decrease rapidly with increasing number of neighbours and does actually vanish for the central atom in the cluster in Fig. 8.8(c). As a result of the decreasing magnetic moments, the exchange interactions decrease as well, which causes the obtained magnetic configurations shown in Fig. 8.8.

The high sensitivity of the magnetic moment of the V atoms towards the coordination number is related to the effect of the band-narrowing which is accompanied with the decreasing number of neighbours. Since V is non-magnetic in the bulk configuration, the Stoner criterion is more difficult to fulfill, and a high coordination number causes the bandwidth to be large enough to stabilize a non-magnetic solution. This is illustrated in Fig. 8.9 where the density of states for the atoms in the ten atom V cluster (shown in Fig. 8.8(c)) is displayed. The leftmost panel shows the DOS for an corner atom. For the edge atoms, for which the DOS are plotted in the middle panel of Fig. 8.9, a larger bandwidth than for the corner atoms is noticed, and in the rightmost panel the DOS for the non-magnetic central atom is shown.

## 8.6 Co on W(001)

Co is a strong ferromagnet in its bulk state and is thus rarely found to have a magnetic coupling that is not ferromagnetic. One exception was mentioned in Sec. 7.2 where the coupling between Co planes in  $\text{TiCo}_2\text{Se}_2$  is non-collinear. Another exception is a Co monolayer on a W(001) surface that, in a recent theoretical study[71], was found to order antiferromagnetically. Motivated by this peculiar behaviour we have studied the magnetic interactions of small Co clusters supported on a W(001) surface. We find that atoms in a nearest-neighbour(NN) dimer couple antiferromagnetically to each other with an exchange coupling  $J_{NN}=-2.9\text{meV}$  and that atoms in next-nearest-neighbour(NNN) dimers couple ferromagnetically with

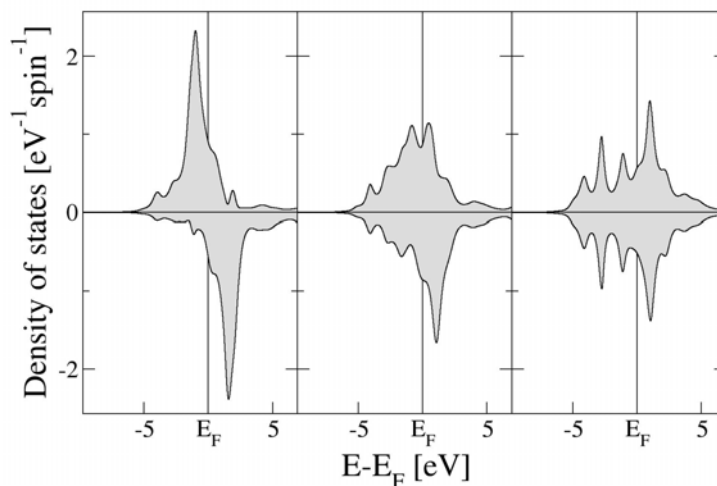


Figure 8.9: Local density of states for atoms in the ten-atom cluster displayed in Fig. 8.8(c).

$J_{NNN}=0.3\text{meV}$ . The magnetic ordering for planar clusters with up to 9 atoms were found to be antiferromagnetic.

More details regarding the magnetic structure of the Co clusters deposited on W(001) can be found in **Paper XVI**.

## 8.7 Cr on Au(111)

With the exception of the Fe clusters on an Ni surface discussed in the previous section, there has been now experimental verification of our calculated magnetic structures. In **Paper XVIII** we have studied the magnetic ordering of small Cr clusters supported on Au(111). The magnetic structure obtained for a triangular Cr cluster is similar to what was found for Cr clusters supported on Cu(111), which was discussed in Sec. 8.4, i.e. a non-collinear ordering with  $120^\circ$  between the magnetic moments of the different Cr atoms. Our calculated structure is in agreement with recent experimental results on the Kondo response[72] for triangular Cr clusters that indicate that these clusters are magnetically frustrated.

---

## 9. Perspectives and outlook

The field of nanomagnetism is still emerging and the continued development of experimental as well as computational methods is important for continuing the current progress. With the non-collinear recursion method presented in this thesis, systems with complex magnetic behaviour can be studied.

The method has already been applied to several systems and show great potential, but it is important to validate the method by comparing obtained results with experiments, or similar theoretical methods, which has only been done to a small extent so far.<sup>1</sup> Unfortunately it is not a trivial task to find ways of comparing the method with experiments. So far the method has been used predominantly for calculating the magnetic ordering of nanoclusters, but even if methods such as spin-polarized STM allow for a resolution of magnetic contrast down to atomic level resolution it is not a simple task to convert these images to a set of directions of magnetic moments or vice versa. A better approach may be to perform more indirect validations by comparing properties that depend on the magnetic configuration instead of measuring the magnetic ordering explicitly. This can for example be done by comparing spectroscopic properties such as the unoccupied density of states.

In a longer perspective, there are also a few improvements that would increase the potential of the method vastly. The first improvement would be to improve the method to go beyond LDA and treat many-body effects more accurately. Due to the localized nature of the electrons in many nanostructures, there is reason to believe that these systems can be strongly correlated. A proper treatment of many-body effects would also make it feasible to analyze the Kondo effect which has been known to occur for small deposited clusters and ad-atoms. Another point on the wish list would be an improvement of the energy resolution so that structural relaxations can be treated to a larger extent. A first step in this direction could be to include full charge-density expansions to improve the ASA resolution. A third improvement would be to extend the method so that free-standing clusters can be treated. Luckily, this third point is currently being adressed.

Regarding the parts of the thesis that are not concerned with nanomagnetism, the density matrix purification implementation opens for interesting possibilities. In contrast to the recursion based method, it can treat non-metallic systems and can thus treat completely different systems. A

---

<sup>1</sup>It is here important to press that the collinear implementation of this method, the RS-LMTO-ASA have been successfully used for more than a decade.

major improvement of this method would be to modify it so that embedded systems can be treated effectively. Similar to the recursion method the density matrix implementation is currently limited by LDA and the LMTO-ASA restrictions.

The recursion method is one of few methods that are equipped to treat amorphous systems reasonably well. Due to the linear scaling of the method and the real-space formulation, realistic amorphous systems can be modelled using thousands of atoms. Small steps have already been taken towards an approach to calculate magnetic interactions in such systems. Continued efforts in this direction may prove very successful in the future.

## 10. Sammanfattning

Det här avhandlingsbladet innehåller ungefär  $2 \cdot 10^{23}$  atomer. Nästan alla dessa atomer har en bulklik omgivning, d.v.s. de befinner sig tillräckligt långt ifrån bladets yta för att påverkas av vad som sker vid gränsskiktet mellan pappret och omgivningen. Skulle bladet bli nästan en miljon gånger tunnare kommer däremot alla atomer befinna sig så nära ytan att deras egenskaper förändras. Dessa förändringar kan förklaras av att symmetrier bryts och att kvantmekaniska effekter påverkar små system starkare än stora. Fenomenet att ett ämnes egenskaper ändras när dess dimensioner krymper är det som utgör basen för nanoteknologin.

De senaste årens nanoteknologiforskning har medfört stora framsteg vad gäller experimentella metoder för att framställa och analysera material av nanostorlek. Med tekniker som t. ex. sveptunnelmikroskopi, kan man manipulera enskilda atomer och mäta deras elektroniska egenskaper. Utvecklingen har också gått framåt när det gäller att tillverka nanostrukturerade material, antingen genom att deponera atomer i tunna skikt, så kallade multilager, eller genom att deponera små klungor av atomer, s.k. kluster, på ytor. Dessa framsteg har gjort det möjligt att till stor del skraddarsy ett materials egenskaper genom att noggrant bestämma materialets kemiska sammansättning och struktur.

Med möjligheten att skapa dessa nanostrukturerade material följer också utmaningen att förstå varför de beter sig som de gör. Förutom experimentella analysmetoder kan även kvantmekaniska beräkningar ge viktig information om materialet. Beräkningsmetoder baserade på täthetsfunktionalteorin, DFT, har visat sig vara mycket effektiva för att analysera och även förutsäga materialegenskaper och de har därför använts med stor framgång de senaste decennierna. När det gäller beräkningar av nanosystem så finns det dock en nackdel med många metoder baserade på DFT, nämligen att de är utvecklade för och anpassade till att användas för system där alla atomer är bulklika.

I den här avhandlingen presenteras en metod som har utvecklats för att beräkna magnetiska egenskaper hos just nanomaterial. Metoden har använts till att beräkna den magnetiska ordningen hos små metallkluster placerade på en metallyta. Det visar sig att geometrin hos dessa kluster spelar stor roll för deras magnetiska egenskaper. På grund av den lägre symmetrin hos en atom i ett ytcluster jämfört med en atom i en bulklik omgivning blir atomernas magnetiska moment större i ytcluster. Det gäller såväl krom som mangan och järn. Den minskade symmetrin kan även göra att ämnen som normalt

sett är omagnetiska, som vanadin och rhodium, blir magnetiska. Atomer av järn och rhodium uppvisar ferromagnetisk ordning, dvs. atomerna vill ordna sina magnetiska moment parallellt med momentet på närliggande atomer. Krom-, mangan- och vanadinatomer vill däremot ordna sina magnetiska moment i motsatt riktning gentemot närliggande atomers moment, i s.k. antiferromagnetisk ordning. Om klustrets geometri är sådan att det inte är möjligt att ordna alla moment antiferromagnetiskt, uppkommer frustration i systemet vilket leder till en ickekolinjär magnetisk ordning, d.v.s. de magnetiska momenten ordnar sig inte längre gentemot en gemensam axel. Exempel på ferromagnetisk, antiferromagnetisk och ickekolinjär koppling kan ses i Fig. 10.1.

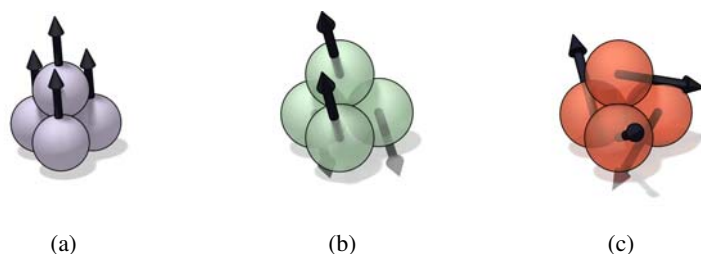


*Figure 10.1:* Magnetisk ordning hos tre nanostrukturer. Den vänstra figuren visar ett järnkluster som har en ferromagnetisk struktur. Bilden i mitten motsvarar ett kromkluster där de magnetiska momenten ordnar sig antiferromagnetisk mot varandra. Den högra bilden visar ett mangankluster där atomernas magnetiska moment inte ordnar sig efter en gemensam axel vilket leder till en ickekolinjär magnetisk struktur.

En tänkbar framtida tillämpning för magnetiska nanokluster är som lagringsmedia i hårddiskar, där man genom att variera klustrets magnetiska struktur kan spara information motsvarande antingen en etta eller en nolla. Ett sådant lagringsmedia skulle kunna motsvara en ökning av lagringstätheten med en storleksordning jämfört med dagens teknik. Magnetiska nanostrukturer i form av järn- och koboltbaserade multilager och inbäddade kluster har undersökts med mål att designa material med så hög magnetiseringstäthet som möjligt. Material med hög magnetiseringstäthet är mycket eftersökta, främst för att användas i skrivhuvud för hårddiskar. Med ett kraftfullt skrivhuvud kan man använda stabilare lagringsmedia än vad som används idag och därigenom öka lagringstätheten. Studien av de järn- och koboltbaserade nanostrukturerna har bidragit till en djupare förståelse av vad som händer med de magnetiska momenten i gränsskiktet mellan de två ämnena. Undersökningarna påvisar ett möjligt klusterbaserat material som kan ha högre magnetiseringstäthet än vad som är känt för andra järn- och koboltlegeringar.

## 11. Acknowledgements

Almost five years ago, I was at the end of my undergraduate studies and looking for a job. A friend (thanks Joa!) suggested that I should contact a professor in a group that I had never heard of. The professor explained the wonders of condensed matter theory in a such enthusiastic way that I really had no choice but to start working with him.

The name of the professor was Olle Eriksson, who I wish to thank for the wonderful supervision and for his always possitive attitude, either regarding the chances of finding fish in brazilian rivers or the possibility of writing two papers on the day of the deadline of the thesis. During these years I have also recieved a lot of help from my assistant supervisor Lars Nordström, without whom I would probably not have understood half of the things I have done.

A large part of this thesis would not have been possible to do withot Sonia Frota-Pessôa who I wish to thank for letting me use her RS-LMTO-ASA method and for patiently explaining the mysteries of the codes (and the input files). I would also like to thank Angela Klautau for a good collaboration with the 'non-collinear' implementation.

Working in this group has been a great pleasure. It is amazing that a bunch of condensed matter theoreticians can have such a nice time together. For this, I would like to thank the father of 'fysikIV' Börje Johansson and all the group members, past and present. Especially I would like to thank my conference buddy Ola, my table-hockey teammate Andreas, my old SN and 04 confederate Björn, my present 04 and 'Johannes' partner Love ,my little greek friend Andreas, my larger greek friend Petros and my former cubicle neighbours Bulten, Carlos, Raquel and Olivier and the rest of the lunch-box gang for all the great times. I would also like to thank the rest of my collaborates: Erik, Lars, Biplab, Till, Torbjörn, Roberto and Frodo, even though the paper is not yet written.

Finally I would like to thank 'klanen Bergman' for all help and support and especially Lotta who makes it all worthwhile.



## Bibliography

- [1] P. Hohenberg and W. Kohn, Phys. Rev. **136**, B864 (1964).
- [2] W. Kohn and L. Sham, Phys. Rev. **140**, A1133 (1965).
- [3] J. Dreizler and E. Gross, *Density Functional Theory, An Approach to the Quantum Many-Body Problem* (Springer, Berlin, 1990).
- [4] V. von Barth and L. Hedin, J. Phys. C. **5**, 1629 (1972).
- [5] J. Kübler, *Theory of Itinerant Magnetism* (Oxford Science Publications, Clarendon Press, 2000).
- [6] L. Nordström and D. J. Singh, Phys. Rev. Lett. **76**, 4420 (1996).
- [7] O. K. Andersen, Phys. Rev. B **12**, 3060 (1975).
- [8] D. D. Koelling and B. N. Harmon, J. Phys. C: Solid State Phys. **10**, 3107 (1977).
- [9] M. S. S. Brooks and P. J. Kelly, Phys. Rev. Lett. **51**, 1708 (1983).
- [10] O. Eriksson, M. S. S. Brooks, and B. Johansson, Phys. Rev. B **41**, 7311 (1990).
- [11] O. Eriksson, B. Johansson, R. C. Albers, A. M. Boring, and M. S. S. Brooks, Phys. Rev. B **42**, 2707 (1990).
- [12] O. K. Andersen, O. Jepsen, and D. Glötzel, *Highlights of Condensed-Matter Theory* (North Holland, New York, 1985).
- [13] O. K. Andersen and O. Jepsen, Phys. Rev. Lett. **53**, 2571 (1984).
- [14] S. Goedecker, Rev. Mod. Phys. **71**, 1085 (1999).
- [15] R. Haydock, *Solid State Physics*, vol. 35 (Academic, New York, 1980).
- [16] R. McWeeny, Rev. Mod. Phys. **32**, 335 (1960).
- [17] L. Råde and B. Westergren, *Mathematics Handbook* (Studentlitteratur, Lund, 1995).

- 
- [18] G. B. Arfken and H. J. Weber, *Mathematical Methods for Physicists* (Academic Press, San Diego, 1995).
- [19] N. Beer and D. Pettifor, *The Electronic Structure of Complex Systems* (Plenum Press, New York, 1984).
- [20] S. Frota-Pessôa, *Phys. Rev. B* **46**, 14570 (1992).
- [21] S. B. Legoas, A. A. Araujo, B. Laks, A. B. Klautau, and S. Frota-Pessôa, *Phys. Rev. B* **61**, 10417 (2000).
- [22] H. M. Petrilli and S. Frota-Pessôa, *J. Phys. Condens. Matter* **2**, 135 (1990).
- [23] C. Nex, *Comp. Phys. Comm.* **53**, 141 (1989).
- [24] K. K. Saha and A. Mookerjee, *J. Phys. Condens. Matter* **17**, 287 (2005).
- [25] A. M. N. Niklasson, *Phys. Rev. B* **70**, 193102 (2004).
- [26] A. M. N. Niklasson, C. J. Tymczak, and M. Challacombe, *J. Chem. Phys.* **118**, 8611 (2003).
- [27] M. Methfessel and J. Kübler, *J. Phys. F* **12**, 141 (1982).
- [28] D. Pettifor, *Bonding and Structure of Molecules and Solids* (Oxford University Press, New York, 1995).
- [29] V. Heine and J. H. Samson, *J. Phys. F* **10**, 2609 (1980).
- [30] V. Heine and J. H. Samson, *J. Phys. F* **13**, 2155 (1983).
- [31] N. W. Ashcroft and N. Mermin (W.B. Saunders, Philadelphia, 1976).
- [32] E. Fawcett, *Reviews of Modern Physics* **60**, 209 (1988).
- [33] S. Halilov, H. Eschrig, A. Perlov, and P. Oppeneer, *Phys. Rev. B* **58**, 293 (1998).
- [34] N. M. Rosengaard and B. Johansson, *Phys. Rev. B* **55**, 14975 (1997).
- [35] A. I. Liechtenstein, M. I. Katsnelson, V. P. Antropov, and V. A. Gubanov, *J. Magn. Magn. Mater* **67**, 65 (1987).
- [36] V. P. Antropov, M. I. Katsnelson, M. van Schilfgaarde, and B. N. Harmon, *Phys. Rev. Lett.* **75**, 729 (1995).
- [37] C. Kittel (Wiley, New York, 1996).
- [38] T. Kasuya, *Prog. Theor. Phys.* **16**, 45,58 (1956).

- 
- [39] K. Yoshida, *Phys. Rev.* **106**, 893 (1957).
- [40] M. D. Stiles, *Phys. Rev. B* **48**, 7238 (1993).
- [41] P. Bruno, *Phys. Rev. B* **52**, 411 (1995).
- [42] M. N. Babich, J. M. Broto, A. Fert, F. N. V. Dau, F. Petroff, P. Eitenne, G. Creuzet, A. Friedrich, and J. Chazelas, *Phys. Rev. Lett.* **61**, 2472 (1988).
- [43] J. S. Moodera, L. R. Kinder, T. M. Wong, and R. Meservey, *Phys. Rev. Lett.* **74**, 3273 (1995).
- [44] P. Weiss and R. Forrer, *Ann. Phys.* **12**, 279 (1929).
- [45] D. I. Bardos, *J. Appl. Phys.* **40**, 1371 (1969).
- [46] M. F. Collins and J. B. Forsyth, *Phil. Mag.* **8**, 401 (1963).
- [47] A. P. Malozemoff, A. R. Williams, and V. L. Moruzzi, *Phys. Rev. B* **29**, 1620 (1984).
- [48] R. H. Victora and L. M. Falicov, *Phys. Rev. B* **30**, 259 (1984).
- [49] K. Schwarz, P. Mohn, P. Blaha, and J. Kübler, *Journal of Physics F: Metal Physics* **14**, 2659 (1984).
- [50] P. Söderlind, O. Eriksson, B. Johansson, R. C. Albers, and A. M. Boring, *Phys. Rev. B* **45**, 12911 (1992).
- [51] G. A. Prinz, *Phys. Rev. Lett.* **54**, 1051 (1985).
- [52] C. Binns, S. Baker, S. Louch, F. Sirotti, H. Cruguel, P. Prieto, S. Thornton, and J. Bellier, *Appl. Surf. Sci.* **226**, 249 (2004).
- [53] E. Holmström, A. Bergman, L. Nordström, I. A. Abrikosov, S. B. Dugdale, and B. L. Gyorffy, *Phys. Rev. B* **70**, 064408 (pages 7) (2004).
- [54] O. Kallenberg (Springer-Verlag, New York, 1997).
- [55] S. H. Baker, C. Binns, K. W. Edmonds, M. J. Maher, S. C. Thornton, S. Louch, and S. S. Dhesi, *J. Magn. Magn. Mater* **247**, 19 (2002).
- [56] C. Binns, *Surface Science Reports* **44**, 1 (2001).
- [57] K. W. Edmonds, C. Binns, S. H. Baker, M. J. Maher, S. C. Thornton, O. Tjernberg, and N. B. Brookes, *J. Magn. Magn. Mater* **220**, 25 (2000).
- [58] S. H. Baker, S. C. Thornton, K. W. Edmonds, M. J. Maher, C. Norris, and C. Binns, *Review of Scientific Instruments* **71**, 3178 (2000).

- 
- [59] S. H. Baker, M. Roy, S. Louch, and C. Binns, *J. Phys. Condens. Matter* **18**, 2385 (2006).
- [60] C. Herring, *Magnetism*, vol. 4 (Academic, New York, 1966).
- [61] L. M. Sandratskii, *J. Phys. Condens. Matter* **3**, 8565 (1991).
- [62] R. Berger, M. Fritzsche, A. Broddefalk, P. Nordblad, and B. Malaman, *J. Alloys. Comp.* **343**, 186 (2002).
- [63] M. van Schilfgaarde, I. Abrikosov, and B. Johansson, *Nature* **400**, 46 (1999).
- [64] Y. Tsunoda, *Journal of Physics: Condensed Matter* **1**, 10427 (1989).
- [65] G. Binnig and H. Rohrer, *Helv. Phys. Acta.* **55**, 726 (1982).
- [66] M. Bode, *Rep. Prog. Phys.* **66**, 523 (2003).
- [67] J.-F. Sadoc and R. Mosseri, *Geometrical Frustration* (Cambridge University Press, Cambridge, 1999).
- [68] P. Kurz, G. Bihlmayer, and S. Blügel, *J. Appl. Phys.* **87**, 6101 (2000).
- [69] P. Kruger, M. Taguchi, and S. Meza-Aguilar, *Phys. Rev. B* **61**, 15277 (2000).
- [70] J. A. T. Costa, R. B. Muniz, and D. L. Mills, *Phys. Rev. Lett.* **94**, 137203 (pages 4) (2005).
- [71] P. Ferriani, S. Heinze, G. Bihlmayer, and S. Blügel, *Phys. Rev. B* **72**, 024452 (pages 4) (2005).
- [72] T. Jamneala, V. Madhavan, and M. Crommie, *Phys. Rev. Lett.* **87**, 256804 (2001).



# Acta Universitatis Upsaliensis

*Digital Comprehensive Summaries of Uppsala Dissertations  
from the Faculty of Science and Technology 167*

Editor: The Dean of the Faculty of Science and Technology

A doctoral dissertation from the Faculty of Science and Technology, Uppsala University, is usually a summary of a number of papers. A few copies of the complete dissertation are kept at major Swedish research libraries, while the summary alone is distributed internationally through the series Digital Comprehensive Summaries of Uppsala Dissertations from the Faculty of Science and Technology. (Prior to January, 2005, the series was published under the title "Comprehensive Summaries of Uppsala Dissertations from the Faculty of Science and Technology".)

Distribution: [publications.uu.se](http://publications.uu.se)  
urn:nbn:se:uu:diva-6763



ACTA  
UNIVERSITATIS  
UPSALIENSIS  
UPPSALA  
2006